Chapter 10

The Greening Earth

Myneni et al.

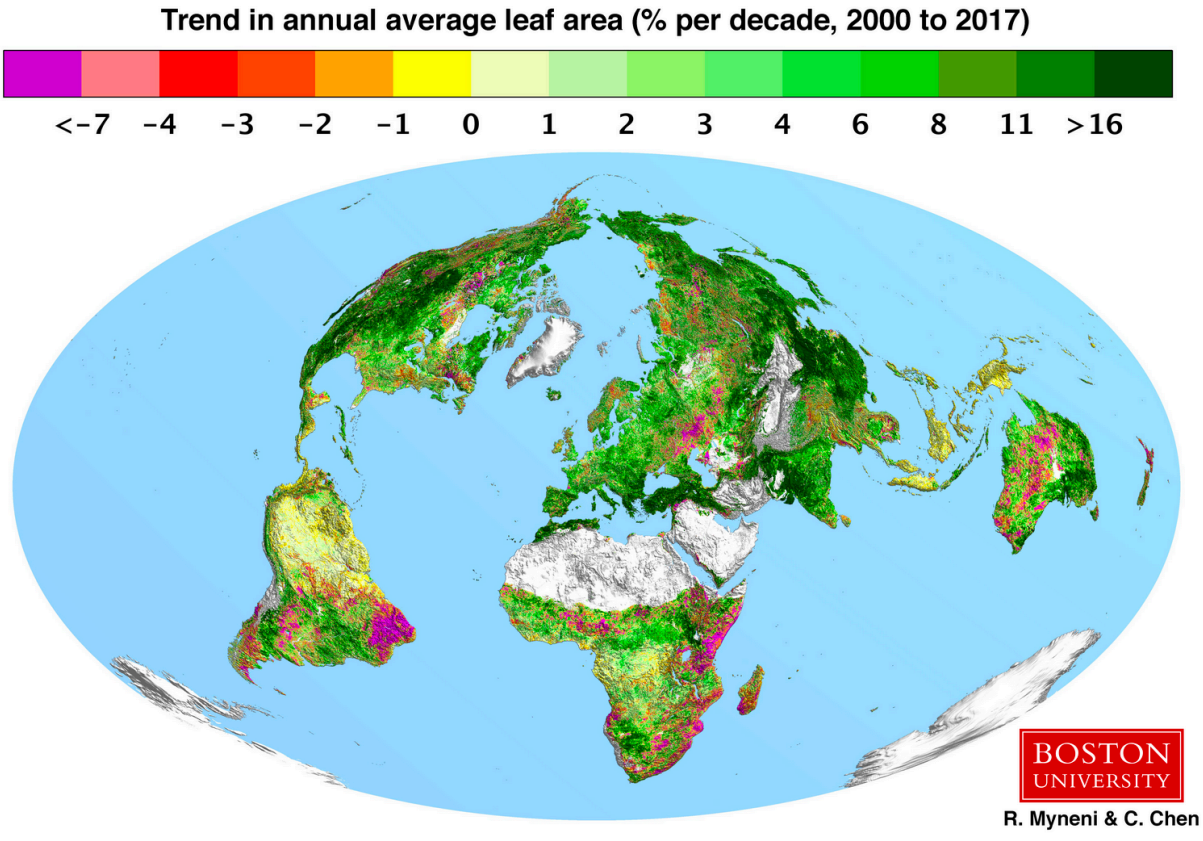

conformational change upon adsorption is observed for Cu–TBPP on Ag(110) (Fig. 3d), where the single adsorption state is characterized by a dihedral angle of 30°.

From this analysis we conclude that the molecular conformation of Cu–TBPP is driven by the nature of the molecule–surface interaction. This conformational adaptation within the molecules occurs in addition to the general tendency for an adsorbate molecular lattice to rotate with respect to the substrate in order to minimize the inequivalent number of adsorption sites[18]. It also goes beyond the observation of a gauche conformation in molecular layers[19]. The saturated hydrocarbon group on the DBP substituents interacts with the surface by a weak chemisorption and permits molecular mobility[13]. Small deviations of the Cu–TBPP conformation ($\sim 90 \pm 10°$) result from modification of the weak chemisorption in response to the atomic corrugation and spacing. In contrast, larger conformational adaptations ($\sim 45°$ and more) are dominated by stronger π–metal interaction at close proximity (typically $\ll 0.5$ nm) of the delocalized electron system of the phenyl and the porphyrin components to the metal.

Conformational analysis of adsorbed molecules permits a semi-quantitative analysis of the adsorbate molecular interaction energy. The degree of rotation of the phenyl–porphyrin bonds balances the intramolecular steric hindrance with the molecule–surface interactions. The rotational barrier for one phenyl–porphyrin bond of tetra-aryl porphyrins in liquids has been measured by thermally activated isomerization of specific isomeric forms (isolated atropisomers) using NMR spectroscopy[20–22] and chromatography. Depending on the central metal atom, substituent and solvent, values of 80–140 kJ per mol per bond[20–22] have been published. This compares favourably with the 100 kJ per mol per bond resulting from a numerical simulation performed for a Cu–TBPP molecule in vacuum[17]. For the 30° dihedral angle observed for Cu–TBPP adsorbed on Ag(110), we estimate an energy of about 320 kJ per mol per bond. This conformation change is accompanied by an increased mixing of the π orbitals of the porphyrin and the phenyls, resulting in reconjugation of π orbitals throughout the molecule. As a result the lateral dimension of the TBP lobes in the STM data for Ag(110) (Fig. 3d) increases, whereas the contrast difference between substituent and centre of the porphyrin decreases to 0.3 nm (compare Cu(100) ~0.8 nm). For comparison, we attempted to perform scanning tunnelling spectroscopy experiments on various parts of the adsorbed porphyrins; but our current–voltage measurements resulted in decay of the molecules, precluding conventional analysis.

STM recognition of the orientation of molecular subunits should provide insights into the detailed geometric factors involved in adsorbent–adsorbate interactions. The conformational changes that we observe reflect the interaction strength of the molecule with the substrate and its geometry. □

Received 27 September 1996; accepted 24 February 1997.

1. Haran, A., Waldeck, D. H., Naaman, R., Moons, E. & Cahen, D. *Science* **263,** 948–950 (1994).
2. Burroughes, J. H. *et al. Nature* **347,** 539–541 (1990).
3. Sheats, J. R. *et al. Science* **273,** 884–888 (1996).
4. Salaneck, W. R. & Brédas, J. L. *Adv. Mater.* **8,** 48–52 (1996).
5. Chen, C. J. *Introduction to Scanning Tunneling Microscopy* (Oxford Univ. Press, New York, 1993).
6. Wiesendanger, R. *Scanning Probe Microscopy and Spectroscopy: Methods and Applications* (Cambridge Univ. Press,, 1994).
7. Seth, J. *et al. J. Am. Chem. Soc.* **116,** 10578–10592 (1994).
8. Bonnett, R. *Chem. Soc. Rev.* **24,** 19–33 (1995).
9. Harima, Y. *et al. Appl. Phys. Lett.* **69,** 1059–1061 (1996).
10. Song, H., Reed, C. A. & Scheidt, W. R. *J. Am. Chem. Soc.* **111,** 6865–6866 (1989).
11. Erler, B. S., Scholz, W. F., Lee, Y. J., Scheidt, W. R. & Reed, C. A. *J. Am. Chem. Soc.* **109,** 2644–2652 (1987).
12. Miyamoto, T. K., Sugita, N., Matsumoto, Y., Sasaki, Y. & Konno, M. *Chem. Lett.* 1695–1698 (1983).
13. Jung, T. A., Schlittler, R. R., Gimzewski, J. K., Tang, H. & Joachim, C. *Science* **271,** 181–184 (1996).
14. Sautet, P. & Joachim, C. *Chem. Phys. Lett.* **185,** 23–30 (1991).
15. Sautet, P. & Joachim, C. *Surf. Sci.* **271,** 387–394 (1992).
16. Chavy, C., Joachim, C. & Altibelli, A. *Chem. Phys. Lett.* **214,** 569–575 (1993).
17. Ercolessi, F., Parrinello, M. & Tosatti, E. *Phil. Mag. A* **58,** 213–226 (1988).
18. Modesti, S., Gimzewski, J. K., Schlittler, R. R. & Chavy, C. *Phys. Rev. Lett.* **72,** 1036–1039 (1994).
19. Rabe, J. P., Buchholz, S. & Askadskaya, L. *Synth. Met.* **54,** 339–349 (1993).
20. Eaton, S. S. & Eaton, G. R. *J. Am. Chem. Soc.* **97,** 3660–3666 (1975).
21. Crossley, M. J., Field, L. D., Forster, A. J., Harding, M. M. & Sternhell, S. *J. Am. Chem. Soc.* **109,** 341–348 (1987).
22. Dirks, J. W., Underwood, G., Matheson, J. C. & Gust, D. *J. Org. Chem.* **44,** 2551–2555 (1979).
23. Gottwald, L. K. & Ullman, E. F. *Tetrahedron Lett.* **36,** 3071–3074 (1969).
24. Hatono, K., Anzai, K., Nishino, A. & Fujii, K. *Bull. Chem. Soc. Jpn.* **58,** 3653–3654 (1985).

Acknowledgements. We thank C. Joachim, H. Tang, P. Guéret and H. Rohrer for enlightening discussions; E. Haskal and W. Riess for discussions and assistance; and K. I. Sugiura, T. Takami and Y. Sakata for synthesizing and providing the molecules. This work was supported in part by the Swiss Federal Office for Education and Science, through the ESPRIT basic research project 'Processing on the nanometer scale (PRONANO)'.

Correspondence and requests for materials should be addressed to T.A.J. (e-mail: thomas.jung@psi.com).

Increased plant growth in the northern high latitudes from 1981 to 1991

R. B. Myneni*, C. D. Keeling†, C. J. Tucker‡, G. Asrar§ & R. R. Nemani‖

* *Department of Geography, Boston University, Commonwealth Avenue, Boston, Massachusetts 02215, USA*

† *Scripps Institution of Oceanography, La Jolla, California 92093-0220, USA*

‡ *NASA Goddard Space Flight Center, Code 923, Greenbelt, Maryland 20771, USA*

§ *Office of Mission to Planet Earth, NASA Headquarters, Washington DC 20546, USA*

‖ *School of Forestry, University of Montana, Missoula, Montana 59812, USA*

Variations in the amplitude and timing of the seasonal cycle of atmospheric CO_2 have shown an association with surface air temperature consistent with the hypothesis that warmer temperatures have promoted increases in plant growth during summer[1] and/or plant respiration during winter[2] in the northern high latitudes. Here we present evidence from satellite data that the photosynthetic activity of terrestrial vegetation increased from 1981 to 1991 in a manner that is suggestive of an increase in plant growth associated with a lengthening of the active growing season. The regions exhibiting the greatest increase lie between 45° N and 70° N, where marked warming has occurred in the spring time[3] due to an early disappearance of snow[4]. The satellite data are concordant with an increase in the amplitude of the seasonal cycle of atmospheric carbon dioxide exceeding 20% since the early 1970s, and an advance of up to seven days in the timing of the drawdown of CO_2 in spring and early summer[1]. Thus, both the satellite data and the CO_2 record indicate that the global carbon cycle has responded to interannual fluctuations in surface air temperature which, although small at the global scale, are regionally highly significant.

We have made use of data from the advanced Very High Resolution Radiometers (AVHRRs) on board the National Oceanic and Atmospheric Administration (NOAA) series of meteorological satellites (NOAA-7, -9 and -11). From daily observations of channel 1 (wavelengths ~0.58–0.68 μm) and channel 2 (~0.72–1.1 μm) reflectances, global land data sets of normalized difference vegetation index (NDVI) were produced[5,6]. The NDVI is expressed on a scale from −1 to +1. It is between −0.2 and 0.05 for snow, inland water bodies, deserts and exposed soils, and increases from about 0.05 to 0.7 for progressively increasing amounts of green vegetation[7]. NDVI data are strongly correlated with the fraction of photosynthetically active radiation (wavelength 0.4–0.7 μm) absorbed by vegetation[8], that is, to the photosynthetic activity of vegetation canopies[9]. Two global data sets of NDVI were analysed: (1) the land segment of the joint NOAA/NASA Earth Observing System AVHRR Pathfinder data set at 8 km spatial resolution and 10-day intervals, for the period July 1981 until the end of June 1991[6], and (2) the Global Inventory Monitoring and Modelling Studies

(GIMMS) AVHRR NDVI data set at a similar spatial resolution, but at 15-day intervals, for the period January 1982 until the end of December 1990[10]. The Pathfinder data were calibrated to correct for post-launch degradation from estimates of the relative annual degradation rates (in %) of the two channels: 3.6 and 4.3 (NOAA-7), 5.9 and 3.5 (NOAA-9) and 1.2 and 2.0 (NOAA-11)[11]. NOAA-9 data were used for inter-satellite normalization. The GIMMS data were independently calibrated[12]; they are considered here to illustrate how a different calibrating scheme affects derived trends in the AVHRR data.

For each equal-area pixel and at either 10- or 15-day intervals, depending on which of the two satellite data sets was used, the maximum of NDVI with minimal atmospheric effects was retained[13]. The NDVI data from high northern latitudes (>40° N) did not show anomalies related to the El Chichon volcanic eruption during the mid-1982 to 1983 time period. These effects in the low latitude data were not corrected for in either of the two satellite data sets.

The calibrated Pathfinder NDVI data still showed residual non-vegetation-related variations[14]. We revised them by adjusting the NDVI for a hyper-arid portion of the Sahara desert (1.42×10^6 km^2) which has been found to be invariant as viewed by all three satellites[10]. An alternate correction scheme based on desert pixels from 10° N to 50° N yielded nearly identical results. Importantly, when this desert correction was applied to the NDVI anomaly time series of desert pixels from five-degree latitude bands between 10° N and 50° N, the residuals resembled noise.

Time series of spatially averaged monthly NDVI, evaluated as the mean of three 10-day maximum value NDVI composites, comprising a 10-year record, are plotted, first directly for reference (Fig. 1a), and then as anomalies to display interannual variability (Fig. 1b). Averaged for regions north of 45° N (uppermost curve in Fig. 1b) the NDVI anomaly shows evidence of increasing amplitude, summer values being low early in the record, high near the end. The NDVI anomaly in the tropics shows a large increase starting from November 1988, which also coincided with the change in satellites from NOAA-9 to NOAA-11. A somewhat smaller increase is seen during the switch from NOAA-7 to NOAA-9 in January 1985, although this increase began in the last months of the NOAA-7 record (and the anomaly north of 45° N actually shows a decrease). This raises a question regarding anomalous variations in NDVI from sensor changes. Although efforts have been made to establish

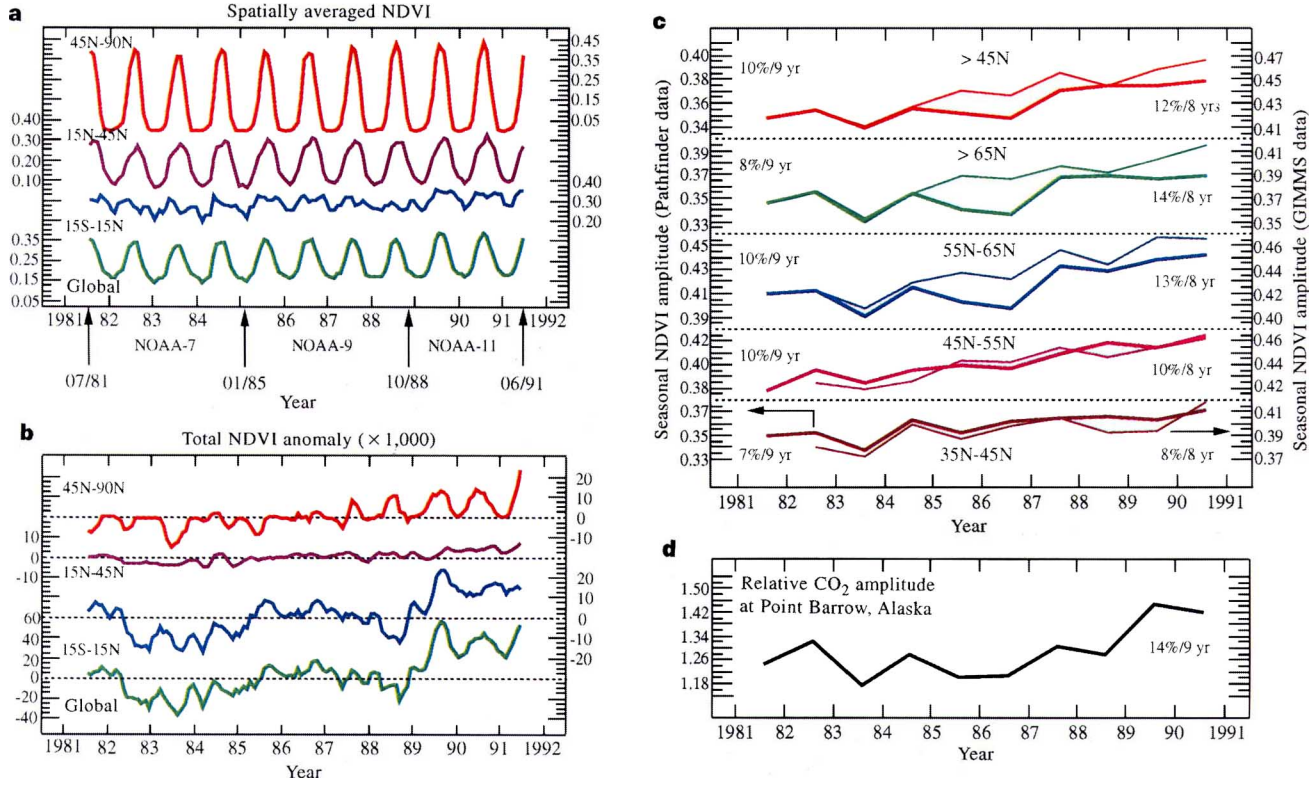

Figure 1 Time variations in normalized difference vegetation index (NDVI) compared with changes in amplitude of the seasonal cycle of atmospheric CO_2 for the period from July 1981 to the end of June 1991. The data in **a** and **b** have been smoothed by a 3-month running mean. Zonal total NDVI and its anomaly were calculated from pixels having a 10-year monthly average NDVI greater than 0.1 and within 3σ of the monthly average. The first condition guaranteed that bare or sparsely vegetated pixels were not included in spatial averages, while the second condition removed most of the influence of snow and bad scan-lines. **a**, Monthly average NDVI for selected latitudinal bands and the whole globe. The zonal total NDVI was normalized by the total vegetated land area in the month of August to obtain a zonal average that exhibited seasonality[14]. **b**, Monthly total anomalies of the above, expressed as departures from the 10-year record averages of monthly NDVI, summed over each latitudinal band[14] for each month. The vertical scale of the global plot is twice that of individual latitudinal bands. **c**, Seasonal amplitude of NDVI averaged over selected latitudinal bands. The amplitude, defined as the July and August average, is a good approximation because, at the northern latitudes shown, the winter-time NDVI value is close to zero. Spatial averaging was for July and August data combined over pixels with 10-year averages of NDVI greater than 0.1, in order to exclude bare areas, such as the great deserts of Asia. Results from both the Pathfinder (left ordinate) and GIMMS (right ordinate) NDVI data sets are shown together with the corresponding rates of increase. The higher rates of increase inferred from GIMMS data may be due to the lack of desert correction for the version of GIMMS data used in this analysis. **d**, Seasonal amplitude of atmospheric CO_2 relative to a base-period of 1961–67 as registered at Point Barrow, Alaska (71° N, 157° W)[1]. Linear trend estimates of the increase in seasonal amplitudes of NDVI and CO_2 are statistically significant (10% level) for all latitudinal bands shown. However, the limitations of regression analysis on short samples, that is, the determination of trend in the presence of low-frequency variations, must be noted.

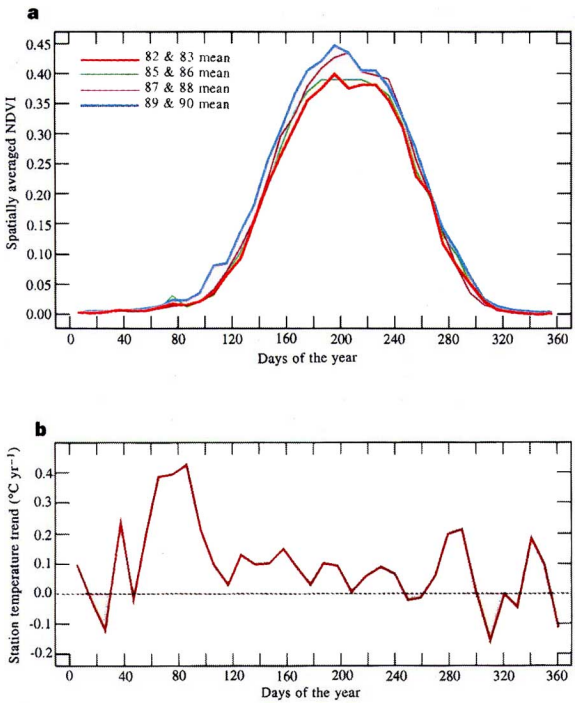

Figure 2 Interannual changes in seasonality of NDVI and in surface temperature, averaged north of 45° N, for selected pairs of years from 1982 to the end of 1900. **a**, NDVI averaged from 10-day maxima in NDVI for 1982–3, 1985–6, 1987–8 and 1989–90. Data from 1984 were not included because the number of years was odd. Spatial averaging was similar to that described in Fig. 1a legend. Changes in the timing of the active growing season over this 9-year record period were estimated from differences between the first and last bi-yearly average profiles at six threshold values of NDVI (from 0.1 to 0.35 in 0.05 increments). These values occurred during intervals of about 60 days each in spring and autumn when, respectively, NDVI was increasing and decreasing, at almost a constant rate. The six estimates each of the timing of rise and fall of NDVI may actually be correlated because of low-frequency variations (for example, soil moisture and/or equatorial sea surface temperature oscillations), and therefore, the standard errors given in the text must be interpreted in light of this limitation. We also inferred similar changes in the active growing season duration from an alternate pixel-by-pixel and year-by-year analysis[14]. **b**, Changes in the annual cycle of near-surface air temperature from 1982 to 1990. Daily thermometer observations of maximum and minimum temperature were averaged in order to approximate daily mean temperatures and interpolated on a 1 × 1 degree grid[22]. The daily data were further averaged over three separate approximately 10-day periods per month to obtain 36 observations per year. These 10-day average temperatures were then linearly regressed on the year (from 1982 to the end of 1990) to obtain the slopes shown here.

proper inter-sensor calibration linkages[11,12], some residual effects cannot be ruled out, especially between NOAA-9 and NOAA-11[14]. This situation, for example, confounds proper interpretation of the tropical NDVI anomaly time series. For instance, intense sea surface temperature (SST) oscillatory events in the tropical Pacific and Atlantic oceans from 1982 to early 1989 have been linked to decreased vegetation growth in large regions of the semi-arid tropics[15]. The increase in tropical and global NDVI anomaly starting from late 1988 also coincided with an unprecedented decline in atmospheric CO_2 anomaly, from a peak value in late 1988 to a minimum in late 1993[16]. Nevertheless, these interpretations, as they involve the NDVI data, are limited by possible sensor change effects.

Changes in the amplitude of the seasonal cycle of NDVI at northerly latitudes greater than 35° N are plotted in Fig. 1c, as characterized by changes in the July and August average NDVI. This broad measure of the seasonal maximum approximates the seasonal amplitude because winter-time NDVI at these northern latitudes is close to zero (compare Fig. 1a). The seasonal amplitude, by this definition, increased by 7 to 14%, depending on the latitude and data set, from 1981 or 1982 to the end of 1990 (Fig. 1c). Because NDVI is a measure of photosynthetic activity of vegetation as noted above[8,9], this increase indicates a substantial change in photosynthetic activity of plants at higher northern latitudes. A similar increase (14%) is indicated in the amplitude of the seasonal cycle of atmospheric CO_2 measured at Point Barrow, Alaska[1] (Fig. 1d). This CO_2 cycle, although observed in the Arctic (71° N), registers changes in CO_2 gas exchanges, and hence in the biotic activity of plants and soil over all northern temperate and polar latitudes[17]. Together, the NDVI and CO_2 data indicate increased biospheric activity north of about 35° N. Two recent studies have also reported increased photosynthetic activity in the northern high latitudes as increased biomass from deposition in European forests[18] and from tree-ring analysis in Mongolia[19], respectively.

Timing of the seasonal rise and fall in NDVI suggests possible changes in the length of the active growing season, that is, the period during which photosynthesis actually occurs (as opposed to the concept of growing season, measured for example in degree days. As shown in Fig. 2a in Pathfinder data, the rise in NDVI, spatially averaged from 45° N to the northern limit of the data, came progressively earlier in the season between 1982 and 1990, as shown by successive 10-day averages, where each plot shows an average over two years for clarity. Because spatially averaged NDVI rose each year at nearly a constant rate from early April (about day 110) to late June (about day 170) the advance in the active growing season is apparent, notwithstanding the relatively coarse time resolution (10 day) afforded by the NDVI data. From six estimates of the time advance at six successive thresholds of NDVI, we estimate an advance of 8 ± 3 days (Fig. 2a).

An advance of about 7 days in the seasonal cycle was previously inferred from atmospheric CO_2 data as having taken place between the 1960s and early 1990s, with most of the increase occurring after 1980 (Fig. 1 of ref. 1). The NDVI data suggest that this increase occurred over an extensive region of the extratropical Northern Hemisphere. The NDVI data in Fig. 2a further indicate a prolongation of the declining phase of the active growing season, estimated at 4 ± 2 days between 1982–3 and 1989–90. Therefore, the active growing season north of 45° N appears to have lengthened by 12 ± 4 days over the 1980s. These estimates must be interpreted as suggestive of a longer active growing season, rather than in an absolute sense, in view of the coarse temporal resolution (10 days) and residual atmospheric effects in NDVI data. The associated standard errors given here are not rigorous, for low-frequency variations in NDVI data invalidate the assumption of statistical independence required of the successive threshold values.

Variations in the amplitude and timing of the seasonal cycle of atmospheric CO_2 have shown an association with surface air temperature consistent with the hypothesis that warmer temperatures have promoted increases in biospheric activity outside the tropics[1,2]. A likely cause is an increase in the length of the active growing season brought about by warmer temperatures[1]. As shown in Fig. 2b, a pronounced increase in late-winter and early-spring temperatures took place over the period of NDVI changes, especially during March.

Because of their high spatial resolution (relative to ground-based meteorological measurements), NDVI data provide spatial detail of where the average changes in amplitude and timing of the active growing season occurred. To address regional variations in NDVI, we show in Fig. 3 a map related to the time plots shown in Fig. 1 together with a map of the 9-year average of NDVI for comparison.

The linear rate of change in NDVI, averaged over the 9 years of

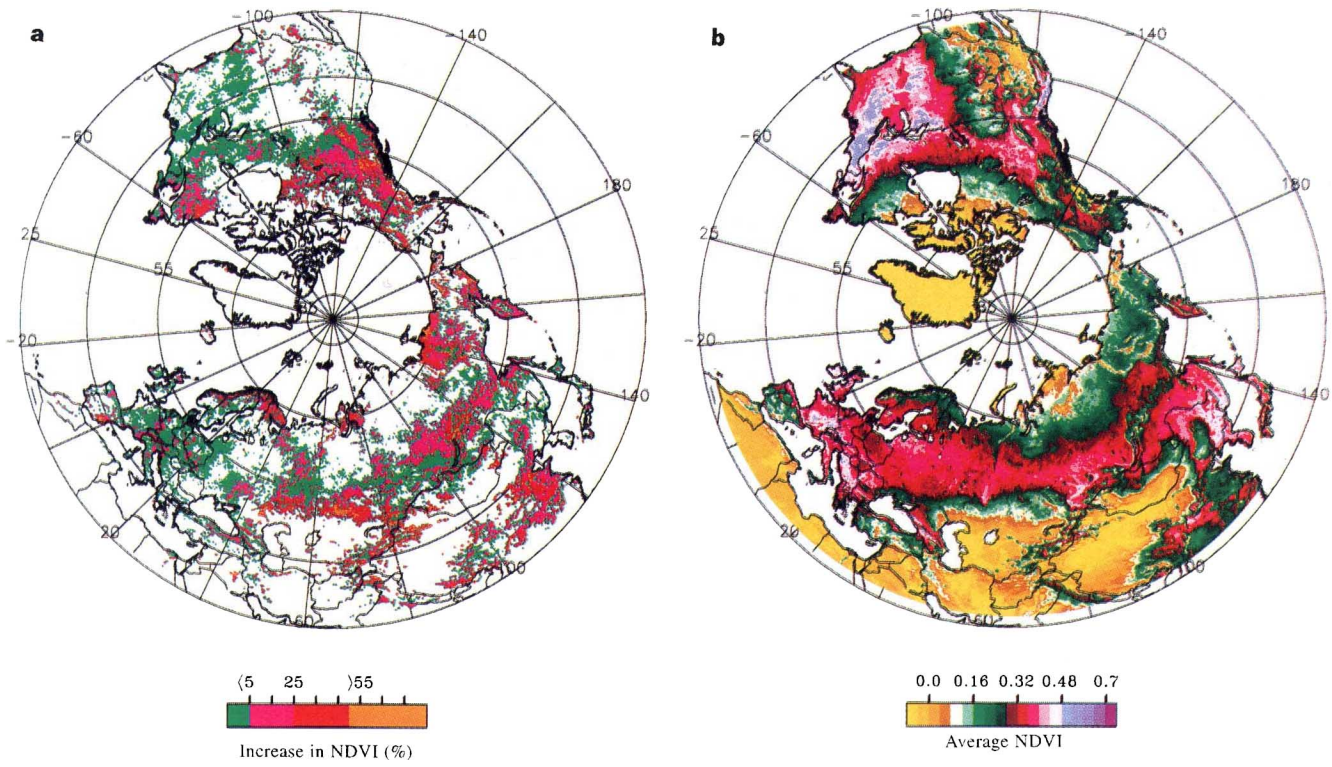

Figure 3 Geographical distribution of the change from 1982 to 1990 in NDVI of land areas north of 27.75° N, expressed as the average over the northern active growing season of May to the end of September. **a**, NDVI increase in percentage over 9 years, determined by linear regression of year-to-year northern growing season averaged NDVI, aggregated to 0.25 × 0.25 degree pixels from original 8-km-resolution data. Only estimates with a positive slope and a statistically significant (10% level) regression coefficient were contoured. There were no pixels with statistically significant negative slopes. Again, we emphasize the limitations of regression analysis on short-term samples. **b**, Nine-year average NDVI over northern active growing season of May to the end of September determined by averaging the monthly NDVI of 0.25 × 0.25 degree pixels from 1982 to 1990.

seasonal NDVI data in northern latitudes, from 1982 to the end of 1990, are mapped in Fig. 3a. Data were averaged from May to the end of September, to approximate the main active growing season of land vegetation in the Northern Hemisphere.

In Eurasia, a band of increasing NDVI extends from Spain in a northeasterly direction across Asia to the western Pacific Ocean. In this band, central Europe, southern Russia, and a broad region near Lake Baikal in Siberia are most affected. Outside this band, northern Scandinavia, northern China, and northeastern Siberia are also strongly affected. In North America, a band of increasing NDVI extends from Alaska in a southeasterly direction to the Great Lakes, thence northeasterly to Labrador. In this band, northwestern Canada is most strongly affected. Outside this band, the continental United States (excluding Alaska) and the area around the Hudson Bay show little change in NDVI.

In general, the regions of greatest increase in NDVI are inland from the oceans, except in the Arctic, and are north of 50° N. The prominent bands of increased NDVI referred to above in both Eurasia and North America, correspond generally to areas of high NDVI (Fig. 3b). Thus most of the areas where changes in NDVI amplitude and seasonality were observed are also regions of significant vegetation density. Notable exceptions are several Arctic regions in Eurasia where NDVI rose sharply from low initial values.

We believe the increasing trend in photosynthetic activity of the northern high latitudes, inferred from satellite observations of NDVI amplitude and phase, to be robust despite varying satellite overpass times and the lack of an explicit atmospheric correction. These effects, however, could modify the magnitudes of NDVI amplitude and estimates of the active growing season duration.

Analyses of station temperature trends during 1961–90 indicate pronounced warming over substantial areas in Alaska, northwestern Canada and northern Eurasia[3]. The greatest warming, up to 4 °C, has occurred in winter. Only slightly less warming has occurred in the same regions in spring, but considerably less warming in summer and even less in autumn[3]. Associated with warming at high latitudes is an approximate 10% reduction in annual snow cover from 1973 to the end of 1992, especially an earlier disappearance of snow in spring (Table 1 of ref. 4). Where snow-lines have retreated earlier due to enhanced warming, we expect an early start of the active growing season.

The winter and spring warming in the interior of the continents of Asia and North America in the 1980s may be a result of natural causes not yet explained, but its timing is consistent with an enhanced greenhouse effect caused by build-up of infrared-absorbing gases in the atmosphere[20]. The unusual warming which peaked near 1990 was of global extent. Although it amounted to a departure of only a few tenths of a degree from previous record temperatures[21], it was associated with far greater warming in the spring months at high northern latitudes. Biospheric activity there, based on our analysis, increased remarkably as a result of this warming, suggesting that small changes in global temperature may reflect disproportionate responses at the regional level, and may be accompanied by positive feedbacks which can markedly influence processes such as photosynthesis and litter decomposition. □

Received 29 August 1996; accepted 3 March 1997.

1. Keeling, C. D., Chin, J. F. S. & Whorf, T. P. Increased activity of northern vegetation inferred from atmospheric CO_2 measurements. *Nature* **382,** 146–149 (1996).
2. Chapin, F. S., Zimov, S. A., Shaver, G. R. & Hobbie, S. E. CO_2 fluctuation at high latitudes. *Nature* **383,** 585–586 (1996).
3. Chapman, W. L. & Walsh, J. E. Recent variations of sea ice and air temperatures in high latitudes. *Bull. Am. Meteorol. Soc.* **74,** 33–47 (1993).

4. Groisman, P. Ya, Karl, T. R. & Knight, T. W. Observed impact of snow cover on the heat balance and the rise of continental spring temperatures. *Science* **263,** 198–200 (1994).
5. Tucker, C. J. in *Advances in the Use of NOAA AVHRR Data for Land Applications* (ed. D'Souza, D.) 1–19 (European Economic Union Press, Brussells, 1995).
6. James, M. E. & Kalluri, S. N. V. The Pathfinder AVHRR land data set: an improved coarse-resolution data set for terrestrial monitoring. *Int. J. Remote Sens.* **15,** 3347–3364 (1994).
7. Tucker, C. J., Fung, I. Y., Keeling, C. D. & Gammon, R. H. Relationship between atmospheric CO_2 variations and a satellite-derived vegetation index. *Nature* **319,** 195–199 (1986).
8. Asrar, G., Fuchs, M., Kanemasu, E. T. & Hatfield, J. L. Estimating absorbed photosynthetic radiation and leaf area index from spectral reflectance in wheat. *Agron. J.* **76,** 300–306 (1984).
9. Myneni, R. B., Hall, F. G., Sellers, P. J. & Marshak, A. L. the interpretation of spectral vegetation indexes. *IEEE Trans. Geosci. Remote Sens.* **33,** 481–486 (1995).
10. Tucker, C. J., Newcomb, W. W. & Dregne, A. E. AVHRR data sets for determination of desert spatial extent. *Int. J. Remote Sens.* **15,** 3547–3566 (1994).
11. Rao, C. R. N. & Chen, J. Inter-satellite calibration linkages for the visible and near-infrared channels of the advanced Very High Resolution Radiometer on the NOAA-7, -9, and -11 spacecraft. *Int. J. Remote Sens.* **16,** 1931–1942 (1995).
12. Los, S. O. Calibration adjustment of the NOAA AVHR Normalized Difference Vegetation Index without recourse to component channel 1 and 2 data. *Int. J. Remote Sens.* **14,** 1907–1917 (1993).
13. Holben, B. N. Characteristics of maximum value composite images for temporal AVHRR data. *Int. J. Remote Sens.* **7,** 1417–1437 (1986).
14. Myneni, R. B., Tucker, C. J., Asrar, G., Keeling, C. D. & Nemani, R. R. Increased vegetation greenness amplitude and growing season duration in northern high latitudes inferred from satellite-sensed vegetation index data from 1981–91. *NASA Tech. Memo. 104638* (NASA Goddard Space Flight Center, Greenbelt, MD, 1996).
15. Myneni, R. B., Los, S. & Tucker, C. J. Satellite-based identification of linked vegetation index and sea surface temperature anomaly areas from 1982–1990 for Africa, Australia and South America. *Geophys. Res. Lett.* **23,** 729–732 (1996).
16. Keeling, C. D., Whorf, T. P., Wahlen, M. & van der Plicht, J. Interannual extremes in the rate of rise of atmospheric carbon dioxide since 1980. *Nature* **375,** 666–670 (1995).
17. Heimann, M., Keeling, C. D. & Tucker, C. J. in *Aspects of Climate Variability in the Pacific and Western Americas* (ed. Peterson, D. H.) 277–303 (Geophys. Monog. Ser., Am. Geophys. Union, Washington DC, 1989).
18. Kauppi, P. E., Mielikainen, K. & Kuusela, K. Biomass and carbon budget of European forests from 1971–1990. *Science* **256,** 70–74 (1992).
19. Jacoby, G. C., D'Arrigo, R. D. & Davaajamts, T. Mongolian tree rings and 20th-century warming. *Science* **273,** 771–773 (1996).
20. Houghton, J. T. *et al.* (eds) *Climate Change 1995* 1–365 (Cambridge Univ. Press, 1995).
21. Jones, P. D., Wigley, T. M. L. & Briffa, K. R. in *Trends '93: A Compendium of Data on Global Change* (eds Boden, T. A., Kaiser, D. P., Sepanski, R. J. & Stoss, F. W.) (ORNL/CDIAC-65, Oak Ridge, TN, 1994).
22. Piper, S. C. & Stewart, E. F. A gridded global data set of daily temperature and precipitation for terrestrial biosphere modelling. *Glob. Biogeochem. Cycles* **10,** 757–782 (1996).

Acknowledgements. We thank S. C. Piper and E. F. Stewart for analysis of the station temperature data, S. C. Piper and T. P. Whorf for discussions, and S. Los for help in the calibration of GIMMS NDVI data. This work was supported by the Office of Mission ot Planet Earth of NASA. E. F. Stewart's collaboration was made possible by funds from the Electric Power Research Institute and the USNSF.

Correspondence should be addressed to R.B.M. (e-mail: rmyneni@crsa.bu.edu).

Large-scale tectonic deformation inferred from small earthquakes

Falk Amelung* & Geoffrey King

Institut de Physique du Globe, 5, Rue Rene Descartes, F-67084 Strasbourg, France

It is a long-standing question whether the focal mechanisms of small earthquakes can be used to provide information about tectonic deformation on a regional scale. Here we address this question by using a 28-year record of seismicity in the San Francisco Bay area to compare the strain released by small earthquakes with geological, geodetic and plate-tectonic measurements of deformation in this region. We show that on a small spatial scale, the strain released by small earthquakes is closely related to specific geological features. But when averaged over a regional scale, strain release more closely follows the regional pattern of tectonic deformation: this relationship holds for all but the largest earthquakes, indicating that the earthquake strain is self-similar[1,2] over a broad range of earthquake magnitudes. The lack of self-similarity observed for the largest earthquakes suggests that the time interval studied is not large enough to sample a complete set of events—the fault with the highest probability[3] for hosting one such missing event is the Hayward fault.

* Present addresses: Department of Geophysics, Stanford University, Stanford, California 94305, USA (F.A.); Institut de Physique du Globe, Laboratoire de Tectonique, Tour 24, BP89, 4 Place Jussieu, 75252 Paris, France (G.K.).

Following the formulation by Kostrov[4], the seismic strain of a block in the Earth's crust can be obtained from the geometric moment tensors

$$\epsilon_{ij} = \frac{1}{2V}\sum_{n=1}^{N} \mathcal{M}_{ij}^{(n)} \qquad (1)$$

where $\mathcal{M}_{ij}^{(n)}$ is the geometric moment tensor of the nth earthquake, N is the number of earthquakes and V is the volume of the block. The geometric moment tensor of an earthquake is given by $\mathcal{M}_{ij} = \int_A u \mathrm{d}A(u_i n_j + u_j n_i)$, where A is the surface of the fault, dA is a surface element, u is the slip in the earthquake, and u_i and n_i are the unit slip and fault-normal vectors, respectively. The geometric moment tensor $\mathcal{M}_{ij}$, referred to by Ben-Menahem and Singh[5] as "potency", is related to the seismic moment tensor M_{ij} used in seismology by $M_{ij} = \mu\mathcal{M}_{ij}$ (ref. 6), where μ is the shear modulus.

The strain in a local region, $\epsilon_{ij}^{(\mathrm{loc})}$, is related to the strain in a larger region, $\epsilon_{ij}^{(\mathrm{reg})}$, by a fourth-order tensor that is a complicated function of time and space. Here we consider special cases in which they are assumed to be linearly related by

$$\epsilon_{ij}^{(\mathrm{loc})} = c\epsilon_{ij}^{(\mathrm{reg})} \qquad (2)$$

where c is the amplitude of the local deformation, that is, the shape and the orientation of the local and regional strain tensors are identical but their amplitudes can be different. For homogeneous deformation, $c = 1$. If seismic strain is self-similar and if $\epsilon_{ij}^{(\mathrm{loc})}$ is the seismic strain by earthquakes in one scale, then equation (2) will apply at any scale with different values for c. Some examples are

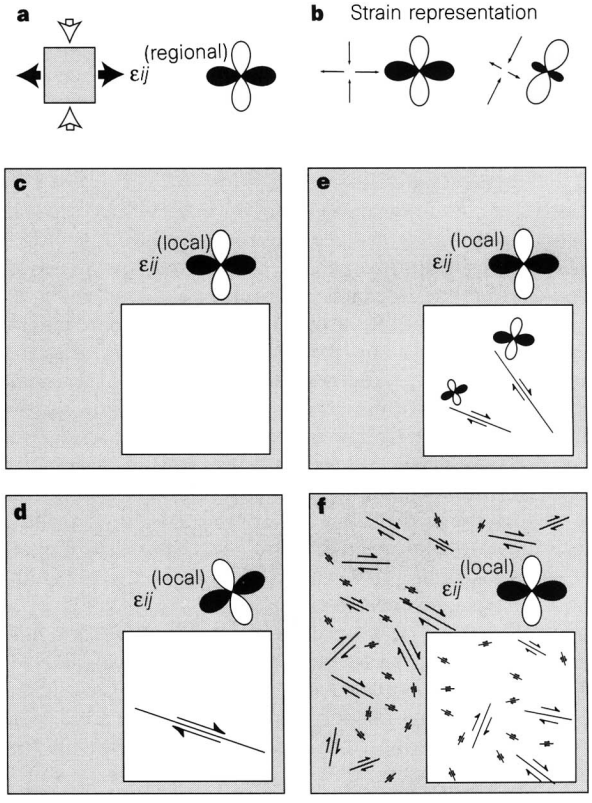

Figure 1 Homogeneous and inhomogeneous deformation in four different regions subject to pure shear. **a**, Boundary conditions and imposed strain. **b**, The strain tensor is represented by two-dimensional strain rosettes for the horizontal components. White lobes indicate directions of contraction, black lobes indicate directions of extensions. **c**, Homogeneous deformation. **d**, Inhomogeneous deformation due to an individual shear fault. **e**, Inhomogeneous deformation due to two faults. **f**, Quasi-homogeneous deformation due to many shear faults with a variety of orientations.

ARTICLES
https://doi.org/10.1038/s41893-019-0220-7
nature sustainability

China and India lead in greening of the world through land-use management

Chi Chen[1*], Taejin Park[1], Xuhui Wang[2], Shilong Piao[2], Baodong Xu[1,3], Rajiv K. Chaturvedi[4], Richard Fuchs[5], Victor Brovkin[6], Philippe Ciais[7], Rasmus Fensholt[8], Hans Tømmervik[9], Govindasamy Bala[10], Zaichun Zhu[11], Ramakrishna R. Nemani[12] and Ranga B. Myneni[1]

Satellite data show increasing leaf area of vegetation due to direct factors (human land-use management) and indirect factors (such as climate change, CO_2 fertilization, nitrogen deposition and recovery from natural disturbances). Among these, climate change and CO_2 fertilization effects seem to be the dominant drivers. However, recent satellite data (2000–2017) reveal a greening pattern that is strikingly prominent in China and India and overlaps with croplands world-wide. China alone accounts for 25% of the global net increase in leaf area with only 6.6% of global vegetated area. The greening in China is from forests (42%) and croplands (32%), but in India is mostly from croplands (82%) with minor contribution from forests (4.4%). China is engineering ambitious programmes to conserve and expand forests with the goal of mitigating land degradation, air pollution and climate change. Food production in China and India has increased by over 35% since 2000 mostly owing to an increase in harvested area through multiple cropping facilitated by fertilizer use and surface- and/or groundwater irrigation. Our results indicate that the direct factor is a key driver of the 'Greening Earth', accounting for over a third, and probably more, of the observed net increase in green leaf area. They highlight the need for a realistic representation of human land-use practices in Earth system models.

The green leaves of vegetation sustain life on Earth by synthesizing sugars from water and CO_2 using the energy of sunlight and cool the surface by transpiring large amounts of water during this process. Their abundance is measured as the one-sided leaf area in broadleaf species and one-half the total needle surface area in coniferous species[1]. This varies seasonally between a maximum of 231×10^6km^2 in July, when the Northern Hemisphere is at its greenest, and a minimum of 132×10^6km^2 in January. The yearly average of 171×10^6km^2 of leaf area found in 109×10^6km^2 of vegetated area represents the annual average leaf area index (LAI) of the Earth—which is 1.57. Greening and browning are defined as statistically significant increases and decreases, respectively, in the annual average green leaf area at a location over a period of several years. Greening or browning could result from changes in the average leaf size, number of leafs per plant, the density of plants, the species composition, duration of green-leaf presence owing to changes in the growing season and multiple cropping.

Data from satellites, available since the early 1980s, indicate increasing greenness over the Earth's lands, from Svalbard to Australia and from Alaska to Chukotka[2–7]. The previously inferred dominant role of a CO_2 fertilization effect[7–11], and of indirect drivers in general[2,7,12–17], in the greening of the Earth raises the question of the role of human land use in shaping the vegetation greenness patterns on global lands. It may be more important than currently thought, for the following reasons. First, the models used in previous attribution analyses had rudimentary representations of evolving complex patterns of land-use practices (described below and elsewhere[18]), thus downplaying the direct role of humans in greening[19]. Second, the effects of higher CO_2 concentrations on plant growth[20], outside of experimental situations, are poorly understood and—as a consequence—the models differ widely in their prognostications[21]. Third, deleterious effects of the loss of sensor calibration, orbital drift of satellites, atmospheric contamination of vegetation signals and disjointed stitching of data from multiple sequential sensors were evident in the underlying satellite data[22] that were used in nearly all previous studies. Fourth, a recent study has shown that human land use is the dominant factor behind changes in woody and herbaceous vegetation cover[23]. Now that better quality leaf area data are available from the moderate resolution imaging spectroradiometer (MODIS) sensor observations[1,24–26]—Supplementary Table 1 describes the specifics of MODIS compared to advanced very high resolution radiometer (AVHRR) data—we aim here to assess the role of the direct driver, that is, human land-use management, without recourse to models, by characterizing the greening patterns in ecosystems globally.

Results

The Earth is greening. According to MODIS data, one-third of the global vegetated area is greening and 5% is browning. This translates to a net increase in leaf area of 2.3% per decade (Fig. 1 and

[1]Department of Earth and Environment, Boston University, Boston, MA, USA. [2]Sino-French Institute for Earth System Science, College of Urban and Environmental Sciences, Peking University, Beijing, China. [3]Macro Agriculture Research Institute, College of Resource and Environment, Huazhong Agricultural University, Wuhan, China. [4]Department of Humanities and Social Sciences, Birla Institute of Technology and Science, Pilani, Goa, India. [5]Institute of Meteorology and Climate Research—Atmospheric Environmental Research, Karlsruhe Institute of Technology, Garmisch-Partenkirchen, Germany. [6]Max Planck Institute for Meteorology, Hamburg, Germany. [7]Laboratoire des Sciences du Climat et de l'Environnement/IPSL, CEA-CNRS-UVSQ, Université Paris Saclay, Gif-sur-Yvette, France. [8]Department of Geosciences and Natural Resource Management, University of Copenhagen, Copenhagen, Denmark. [9]Norwegian Institute for Nature Research, Fram Centre, Tromsø, Norway. [10]Center for Atmospheric and Oceanic Sciences, Indian Institute of Science, Bangalore, India. [11]Shenzhen Key Laboratory of Circular Economy, Shenzhen Graduate School, Peking University, Shenzhen, China. [12]NASA Ames Research Center, Moffett Field, CA, USA. *e-mail: chenchi@bu.edu

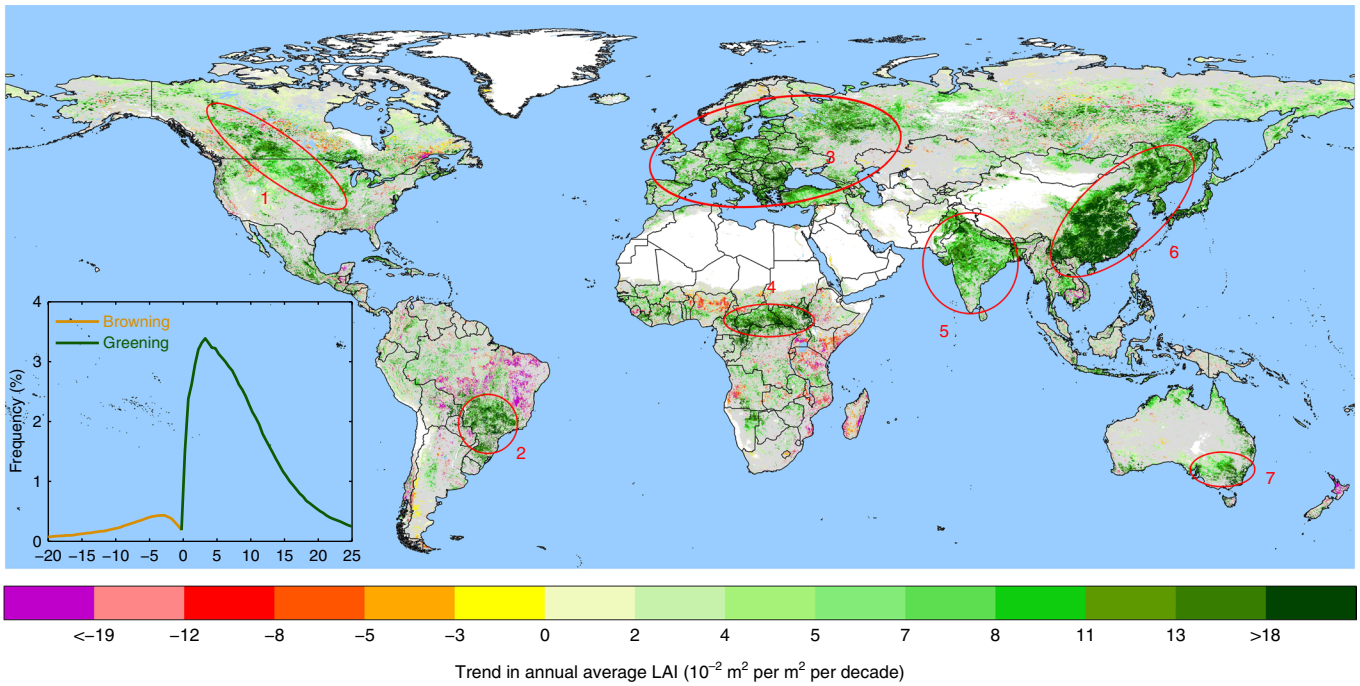

Fig. 1 | Map of trends in annual average MODIS LAI for 2000–2017. Statistically significant trends (Mann–Kendall test, $P \leq 0.1$) are colour-coded. Grey areas show vegetated land with statistically insignificant trends. White areas depict barren lands, permanent ice-covered areas, permanent wetlands and built-up areas. Blue areas represent water. The inset shows the frequency distribution of statistically significant trends. The highlighted greening areas in red circles mostly overlap with croplands, with the exception of circle number 4. Similar patterns are seen at $P \leq 0.05$ and the seven greening clusters are visible even at $P \leq 0.01$.

Table 1 | Net changes in leaf area (10^{-1} million km^2) for the period 2000–2017

	Forests	Other woody vegetation	Grasslands	Croplands	All vegetation
Global	16.72	11.50	7.85	17.85	53.91
By latitude					
>50° S or N	4.78	3.48	0.80	2.36	11.41
25° S–50° S and 25° N–50°N	8.87	3.38	4.61	10.76	27.62
25° S–25° N	3.08	4.64	2.44	4.73	14.88
By MAT					
MAT <10 °C	7.48	3.61	4.04	5.23	20.36
MAT = 10–25 °C	7.92	5.82	2.46	7.70	23.89
MAT >25°C	1.32	2.06	1.35	4.92	9.65
By ATP					
ATP <500 mm	1.76	4.08	3.86	2.66	12.35
ATP = 500–1,000 mm	7.37	2.29	1.30	9.23	20.20
ATP >1,000 mm	7.59	5.13	2.69	5.95	21.35

Net changes were calculated as the difference between greening and browning for the period 2000–2017.

Supplementary Table 2), which is equivalent to adding 5.4×10^6km^2 of new leaf area over the 18-year period of the record (2000 to 2017; Table 1). Two-thirds of this greening is from croplands and forests in about equal measure (Supplementary Table 3). The greening is prominently clustered in seven regions across six continents—most notably in China and India (Fig. 1), which together account for nearly one-third of the observed total net increase in green leaf area globally (China 25% and India 6.8%, Tables 1 and 2). This greening is seen over 65% of the vegetated lands in the two countries (Supplementary Table 4).

We compare the above results to those from AVHRR data[7], which we have recently updated using the same method described previously[27], for completeness. AVHRR data from the comparable period (2000–2016) show less greening (22% of vegetated lands) and more browning (14%) (Supplementary Table 2). Nearly 60% of the net increase in leaf area is from croplands, whereas forests show a net decrease (Supplementary Table 3). Of the seven greening clusters in MODIS (Fig. 1), six approximately match to the AVHRR data, albeit with lower spatial extents and weaker magnitudes, and the sub-Saharan cluster is missing from the AVHRR analysis

Table 2 | Ranking of the 11 largest countries by leaf area and its change during 2000–2017

Rank	Annual average leaf area in 2000 (million km²)	Net change in leaf area (10^{-1} million km²)	Net change in leaf area (%)
1	Brazil (29.68)	China (13.51)	China (17.80)
2	Russia (12.36)	Russia (7.57)	India (11.10)
3	United States (8.93)	EU (4.02)	EU (7.78)
4	Indonesia (8.69)	India (3.65)	Canada (7.13)
5	DRC (8.50)	United States (3.59)	Russia (6.62)
6	China (7.64)	Canada (3.35)	Australia (5.62)
7	Canada (5.41)	Australia (2.83)	United States (4.55)
8	EU (5.23)	Brazil (1.12)	Mexico (4.07)
9	Australia (5.19)	Mexico (0.96)	Argentina (1.70)
10	India (3.33)	DRC (0.96)	Brazil (1.54)
11	Mexico (2.66)	Indonesia (0.51)	DRC (1.34)
12	Argentina (2.16)	Argentina (0.13)	Indonesia (0.83)

The following large countries were excluded because of unfavourable climatic conditions for vegetation growth: Algeria, Denmark (which includes Greenland), Kazakhstan and Saudi Arabia. The EU is included here, although it is not a country. DRC, Democratic Republic of the Congo.

Table 3 | Ranking of the 11 largest countries by vegetated land area and proportion of vegetated lands that show statistically significant trends

Rank	Vegetated land area (million km²)	Proportion of vegetated lands showing greening (%)	Proportion of vegetated lands showing browning (%)
1	Russia (16.04)	India (69.0)	Brazil (11.6)
2	United States (8.91)	China (65.6)	Indonesia (6.8)
3	Canada (8.47)	EU (51.4)	Argentina (6.7)
4	Brazil (8.31)	Canada (41.6)	Canada (5.7)
5	Australia (7.50)	Russia (38.0)	DRC (4.5)
6	China (7.19)	United States (33.3)	United States (2.9)
7	EU (4.22)	Mexico (28.4)	Russia (2.7)
8	India (2.94)	Brazil (25.6)	Mexico (2.4)
9	Argentina (2.57)	Australia (24.4)	China (1.3)
10	DRC (2.28)	DRC (23.7)	EU (1.3)
11	Mexico (1.88)	Indonesia (19.7)	Australia (0.8)
12	Indonesia (1.80)	Argentina (13.2)	India (0.8)

The following large countries were excluded because of unfavourable climatic conditions for vegetation growth: Algeria, Denmark (which includes Greenland), Kazakhstan and Saudi Arabia. The EU is included here, although it is not a country.

(Supplementary Fig. 1a). The data from the two sensors agree on the magnitude of greening in China and India (Supplementary Table 4), probably because of the lower base LAI values (Table 2), larger spatial extents of greening (66 and 69%, respectively; Table 3) and higher relative changes in leaf area (18 and 11%, respectively; Table 2). Globally, LAI trends from the two sensors agree over 61% of the vegetated area and the disagreement is mostly in tropical humid areas and at Northern high latitudes, where the quality of the AVHRR data is poor (Supplementary Fig. 3). The full AVHRR record (1982–2016) shows more greening (41%) and browning (11%) in comparison to the shorter MODIS record, and the patterns exhibit both similarities (red circles in Supplementary Fig. 1b) and important differences (blue circles). The two are not expected to be comparable, although both point to a Greening Earth[2–7]. These results are consistent with recent independent estimates of changes in woody and herbaceous cover[23].

Human land use is a dominant driver of the Greening Earth. The above results provide at least four arguments in favour of a greater role for a direct human driver than previously thought[2,7,12]. First, cropland greening contributes the most to the net increase in leaf area globally since 2000 (33%, Table 1). Six out of seven greening clusters (Fig. 1) overlap with the areal pattern of agricultural primary productivity that has previously been derived independently[28] (Supplementary Fig. 2). Cropland greening is mainly attributable to the direct driver, without discounting the minor but opposing[29,30] contributions of the indirect drivers (CO_2 fertilization has been reported to increase crop production, whereas climate change has been reported to increase or decrease crop yields depending on the location). The green revolution can be attributed to quick-growing hybrid cultivars, multiple cropping, irrigation, fertilizer use, pest control, better quality seeds, farm mechanization, credit availability and crop insurance programmes[31]. Second, the suggestion that the CO_2 fertilization effect on greening should be seen prominently in hot and arid environments, where water limits plant growth[9,20], is not apparent in our analysis. Overall, greening of natural vegetation from these regions (a mean annual temperature (MAT) greater than 25 °C of 13% and an annual total precipitation (ATP) less than 500 mm of 27%) contributes much less than those from mild (MAT < 25 °C, 87%) and wet (ATP > 500 mm, 73%) climates (Table 1)—this is also true when Table 1 entries are adjusted for vegetated area in each climate class. Third, compared to indirect drivers, gains from cropland production in the northern temperate regions, which overlap with the greening patterns presented here (Table 1), contribute more toward explaining the increasing amplitude of the seasonal cycle of atmospheric CO_2 concentration[32]. Finally, the large contribution of northern temperate forests to global net greening (16%, Table 1) indicates that large-scale tree plantations in previously low-productive areas of China and silvicultural practices in developed countries are important, further highlighting the role of the direct driver.

To further appreciate the importance of human land-use management in greening the world, we compare the trends in 11 large countries with sizeable populations and vegetated lands (Table 3). China and India stand out. They are the two most populous countries, but rank in the middle in terms of vegetated area. For this reason, and also because they are situated in temperate to subtropical climes, they rank either in the middle (China) or towards the bottom (India) in terms of annual average leaf area (Table 2). However, they rank at the top (and bottom) in terms of proportion of vegetated lands that exhibits greening (and browning; Table 3). As a consequence, they occupy the top ranks in terms of net increase in leaf area, both on an absolute and relative basis (Table 2). China alone accounts for 25% of the global net increase in leaf area with only 6.6% of global vegetated area. This is equal to the net greening in the three largest countries, Russia, the United States and Canada, that together hold 31% of the global vegetated area (Tables 1–3). India is similarly noteworthy. It ranks first (and last) in terms of the proportion of vegetated area that exhibits greening (and browning; Table 3). With only 2.7% of the global vegetated area, India accounts for 6.8% of the global net increase in leaf area, which is equal to that in the United States or Canada, each of which has three times more vegetated area. This statistic is even more remarkable considering that the annual average leaf area of India is two to three times smaller than that of Canada and the United States, respectively (Tables 2 and 3).

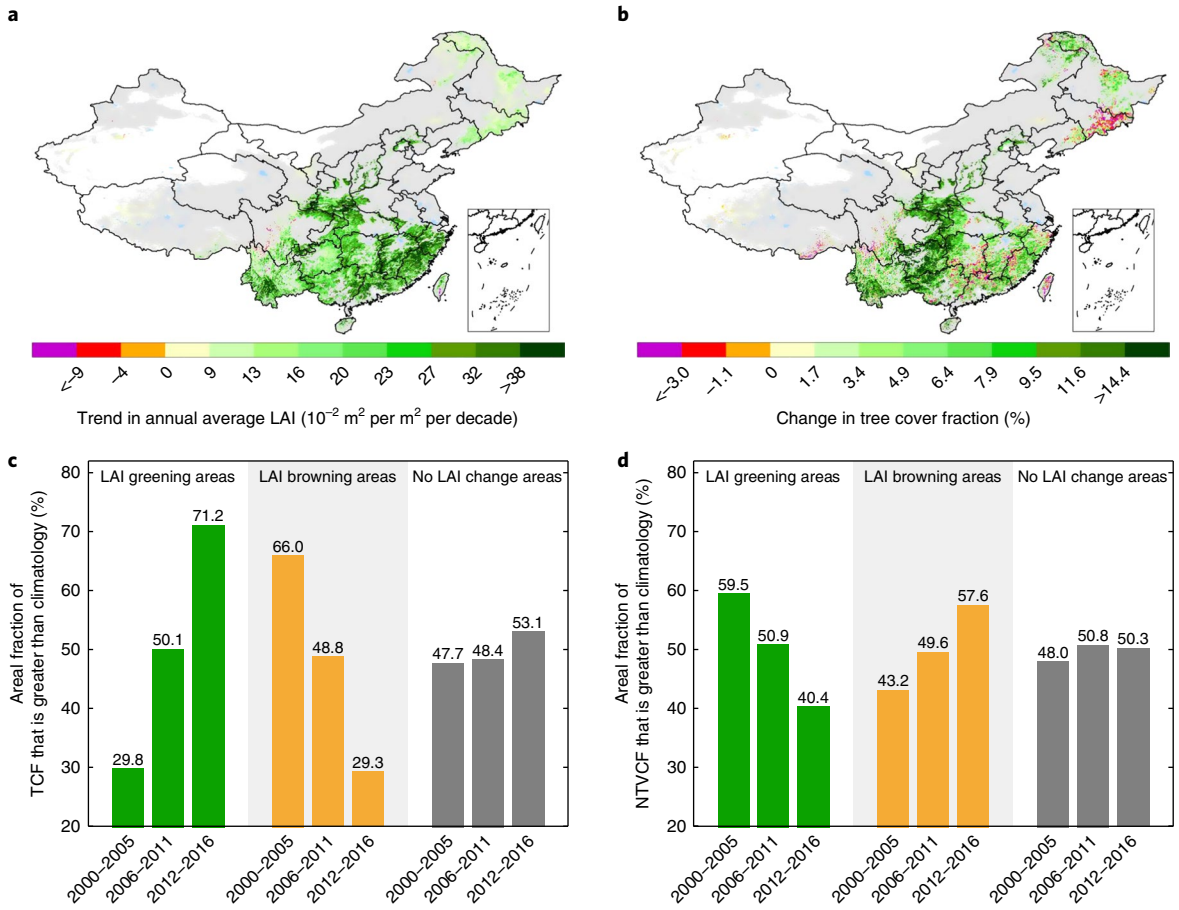

Fig. 2 | Trends in forests and other woody vegetation of China. a, Trend in annual average LAI of forests and other woody vegetation. **b**, Change in the fraction of tree cover in forests and areas of other woody vegetation between 2014–2016 and 2000–2002 in areas that show statistically significant LAI trends in **a**. Grey areas show vegetated land with statistically insignificant LAI trends or predominantly herbaceous vegetation. White areas depict land that is not vegetated. Black lines are boundaries of the first-level administrative divisions. **c**,**d**, Areal fraction of tree cover fraction (TCF) (**c**) and non-tree vegetation cover fraction (NTVCF) (**d**) over forests and other woody vegetation that is greater than the climatology during a particular period, that is, 2000–2005, 2006–2011 and 2012–2016. Climatology is the mean of values from long-term observations. The colours further confine the analysis to areas of LAI greening (green bars), browning (browning bars) and no LAI change (grey bars).

The European Union (EU) lands deserve a special mention in view of the prominent greening pattern in Fig. 1 (circle 3). This region, like China, ranks in the middle in terms of vegetated land area (Table 3) and average annual leaf area (Table 2) among the large countries studied here. Similar to China, it ranks at the top (third) in terms of vegetated lands that exhibit greening and towards the bottom for browning. These changes produce a top rank for this region for net increase in leaf area (third)—55% of which is due to croplands and 34% to forests (nearly all forests are managed in the EU). Recent studies traced the greening in European semi-natural vegetation to land-use practices, principally land abandonment and afforestation[33–35]. Brazil, on the other hand, ranks towards the bottom, because the greening from croplands and pastures is nearly offset by the browning of forests and cerrado[23]. The dominant cropland contribution to expansive greening in China, India, the EU and the United States, highlights the importance of the direct driver in global greening.

China and India lead in the greening of the Earth. We next investigated what factors explain the large-scale greening of China and India in the twenty-first century. Forests and croplands contribute 42% and 32%, respectively, to the net increase in leaf area of China whereas croplands alone contribute 82% in the case of India (the contribution of forests in India is minor, 4%, and was therefore not discussed in detail). Focusing first on forested lands in China, we note an increase (or decrease) in tree (or non-tree) cover in the greening areas (84% of all forests and other wooded lands) and the opposite in the few (<1%) browning areas (Fig. 2). Forest inventories reveal a 19% increase in forest area ($330 \times 10^3 km^2$) in a single decade because of expanding natural forests and afforestation, in equal measures (Supplementary Table 5). China is implementing several ambitious programmes[36] to conserve and expand forests with the goal of mitigating soil erosion, air pollution and climate change (Supplementary Table 6). Already a third of the $2.08 \times 10^6 km^2$ of current forests are plantations (Supplementary Table 5) with rapidly growing young trees that are less than 40 years old[37]. For example, the mean LAI trend ($0.23\,m^2$ per m^2 per decade) for regions with a planted forest fraction (PFF) ≥ 10% is 53% greater than the mean LAI trend ($0.15\,m^2$ per m^2 per decade) for regions with PFF < 10%. Similarly, the mean tree cover trend (6.18% per decade) for regions with PFF ≥ 10% is 29% greater than the mean tree cover trend (4.90% per decade) for regions with PFF < 10%. Other recent studies attest to the success of these programmes in terms of ameliorating land degradation[38], lowering surface temperatures[39] and facilitating carbon sequestration[40], but a strain on water resources has also been noted[41]. All of this emphasizes the importance of human actions for the greening of the wooded lands of China.

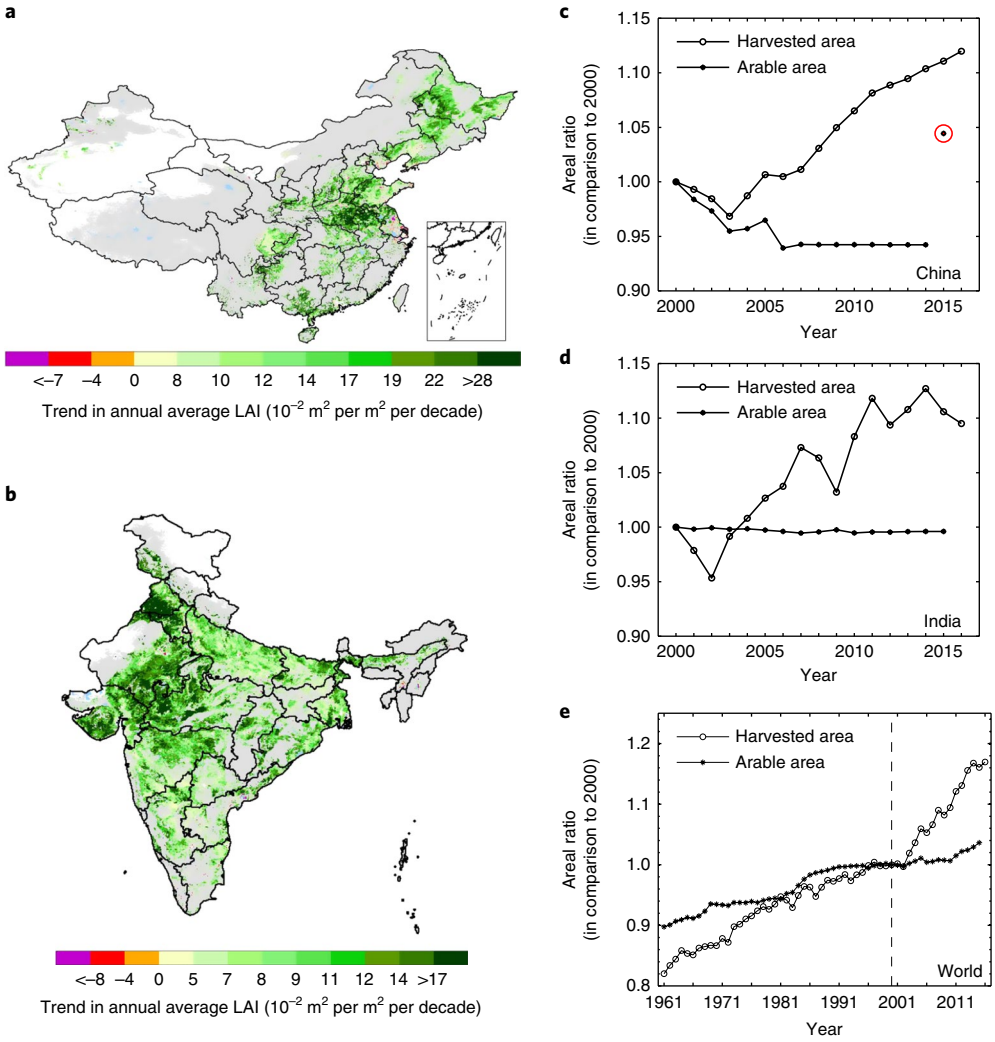

Fig. 3 | Leaf area trends in croplands of China and India. a,**b**, Trend in annual average LAI in croplands in China (**a**) and India (**b**). **c**–**e**, Ratio of harvested area (circle) and arable area (asterisk) with respect to 2000 values for China (**c**), India (**d**) and the world (**e**). The asterisk circled in red in **c** is an outlier. The vertical dash line in **e** indicates 2000.

A recent study[42] has reported browning trends in natural vegetation of India using MODIS normalized difference vegetation index (NDVI) data, but our reanalysis of the same data does not support this conclusion. The previous study[42] focused exclusively on the 8% and 4% browning proportions in forests and other woody vegetation classes while ignoring the 19% and 48% greening proportions in these two classes, during the period of their investigation (2001–2014; Supplementary Table 7). The greening proportions increase to 47% and 55% and the browning proportions decline to 1% and 0.5% for the full record (2000–2017). The browning during the shorter period (2001–2014) spans about 42,300 km^2 and is comparable to the previously published[42] estimate of 55,000 km^2. However, this decreases to 5,000 km^2 during the full record (2000–2017). Greening, on the other hand, is seven times greater (283,300 km^2) during the shorter period and increases to being 80 times greater (401,800 km^2) for the full record. An independent study[43] of trends in MODIS vegetation indices confirms our results.

With regards to cropland greening in China and India, we note that the two countries had comparable and stable land areas under crop cultivation since 2000 (about 1.92 and 2.11 × 10^{6}km^2, respectively, Fig. 3). Still, total food production (for example, grains, fruits and vegetables) has increased significantly (by 35% to 40%) according to our analysis of data from the Food and Agriculture Organisation[44] ((FAO); Supplementary Table 8). For example, the total cereal production in China has increased by 43% from 407 × 10^{6}tonnes in 2000 to 583 × 10^{6}tonnes in 2016. Although yields in India are lower, total cereal production increased by 26% during the same period (from 235 to 295 × 10^{6}tonnes). This is largely because of the increase in harvested area through multiple cropping[45] (Fig. 3), which results in the observed greening trends. Agricultural intensification in China and India is being facilitated by heavy fertilizer use[46] and surface- and/or groundwater irrigation[47,48]—the two currently rank at the top for the amount of fertilizer use (Supplementary Table 7). Harvested land area at the global scale grew approximately four times faster than the cropland area since 2000 in large part due to these practices in China, India and Brazil[45] and this is reflected in the MODIS greening patterns (Fig. 1). Of particular interest is the leading and impressive relative changes in agricultural production, fertilizer use and harvested area in Brazil; however, this is due to starting from lower base values (Supplementary Table 8). The observed large-scale greening of China and India is a harbinger of food self-sufficiency for 2.7 billion people in the two top ranked countries in terms of agricultural output (nominal gross domestic product of US$1.1 and 0.41 trillion, respectively, in 2015 from the agricultural sector in 2015 according to the CIA World Factbook).

Concluding remarks. A third of the global vegetated lands are currently greening—that is, becoming more productive—in a pattern that is reflective of intensive human use of land for crops and forests across all continents, but most prominently in the two populous countries China and India. This suggests that human land-use management is an important driver of the Greening Earth[2–7], accounting for a third, and probably more, of the observed net increase in green leaf area. Therefore, one of the priorities for Earth System Model refinement is a realistic representation of the spatio-temporal dynamics of key land-use practices—multiple cropping, irrigation and fertilizer use, fallowing and abandonment of land, afforestation, reforestation and deforestation. Although human exploitation of land will remain a complex dynamic endeavour, monitoring this using spaceborne datasets, especially high-spatial-resolution data, may offer insights into how this may be realistically represented in models. Finally, it is important to note that the gain in greenness, which mostly occurred in the Northern temperate and high latitudes, does not offset the damage from loss of leaf area in tropical natural vegetation (for example, in Brazil, Democratic Republic of the Congo and Indonesia; Tables 2 and 3) and attendant consequences for ecosystem sustainability and biodiversity.

Methods

MODIS LAI product. Collection 6 (C6, also version 6) Terra and Aqua MODIS LAI products (MOD15A2H and MYD15A2H) are used in this study[49,50]. These LAI datasets are provided as 8-day composites with a 500-m sinusoidal projection covering the whole globe. They are further refined by rigorous checking of the quality flags of the LAI products and of the simultaneous vegetation index products, following the previously described methods[51]. This filtering provides the highest quality MODIS LAI observations that minimize any residual contamination from clouds, aerosols, snow and shadow. The two LAI datasets (that is, four 8-day composites) are then combined into a 16-day composite by taking the mean of all valid LAIs (temporal average). They are then spatially aggregated to generate 0.05° data in a climate-modelling grid ((CMG); the spatial average). The remaining gaps, although very few, are filled using the climatology of each 16-day composite during 2000–2017. Finally, the annual average LAI for each 0.05° pixel is calculated and used in this study.

The quality of C6 MODIS LAI datasets was comprehensively evaluated against ground-based measurements of LAI and through intercomparisons with other satellite LAI products[24,25]. These datasets represent the latest and highest quality LAI products that are currently available. They result from two decades of research on the LAI algorithm development, testing, refinement and validation—these efforts are described in over 50 peer-reviewed journal articles listed at the MODIS Land validation website[52].

AVHRR LAI3g product. We generated a new version of the LAI data (LAI3gV1) as part of this study based on the previously described methodology[27]. It has global coverage with bimonthly frequency and has a 1/12° spatial resolution. It spans the period July 1981 to December 2016. It is the longest among current LAI datasets. The full time series of LAI3gV1 data was generated by an artificial neural network algorithm that was trained with the overlapping data (2000–2016) of NDVI3gV1 and C6 Terra MODIS LAI datasets. Here, NDVI3gV1 refers to the new version of the third-generation normalized difference vegetation index data provided by Global Inventory Modeling and Mapping Studies (GIMMS) AVHRR[53]. The annual average of LAI3gV1 is calculated from 24 observations per year.

AVHRR LAI data prior to 2000 are not evaluated as required field data are not available. Ground data collected as part of MODIS validation efforts after 2000 were used to test the quality of AVHRR LAI data and these have been described previously[27].

MODIS land cover type product. The land cover information is provided by the collection 5.1 MODIS yearly product known as MCD12C1[54]. The spatial resolution of land cover is 0.05° in CMG. The International Geosphere-Biosphere Programme (IGBP) classification types provided by MCD12C1 are aggregated into four broad biome types in this study—forests, other woody vegetation, grasslands and croplands. Forests include evergreen needleleaf forest, evergreen broadleaf forest, deciduous needleleaf forest, deciduous broadleaf forest and mixed forest. Other woody vegetation includes closed shrublands, open shrublands and woody savannahs. Grasslands include savannahs and grasslands. Croplands include croplands and mosaics of croplands and natural vegetation. A static land cover map (that is the map for 2007) is used to define the above-mentioned four broad biome types.

MODIS vegetation continuous field product. C6 Terra MODIS vegetation continuous field is a yearly product that presents a continuous, subpixel fraction of land surface cover with a 250-m sinusoidal projection from 2000 to 2016[55]. The fraction of land surface cover has three components, which include the percentage of tree cover, percentage of non-tree vegetation cover and percentage of non-vegetated cover. The 250-m data are aggregated to 0.05° CMG in this study.

Temperature and precipitation data. Monthly 0.5° CMG temperature and precipitation data are provided by the University of East Anglia Climate Research Unit (CRU) and the latest version is CRU TS4.01[56]. MAT and ATP were calculated for each year. The climatology of the MAT and ATP is also evaluated during the period of 2000 to 2016. Three climatic zones were defined based on the climatology of MAT: (1) cool, MAT < 10 °C; (2) warm, MAT = 10–25 °C; and (3) hot, MAT > 25 °C. Another three climatic zones were defined based on the climatology of ATP: (1) dry, ATP < 500 mm; (2) wet, ATP = 500–1,000 mm; and (3) humid, ATP > 1,000 mm.

Data on country administrative areas. Data on country administrative areas was obtained from the Database of Global Administrative Areas (GADM) hosted by University of California at Davis (https://gadm.org/). The GADM data provide high-resolution shapefiles at all administrative levels, such as at the country, state or provincial level (https://gadm.org/). We used the latest version (v.2.8) in this study.

FAOSTAT database. Arable area, harvested area, cereal production and population were obtained from the FAOSTAT database hosted by the FAO[44]. Crop statistics (that is, arable area and harvested area) are recorded for 173 types of crops from 1961 to 2015/2016. Arable area and harvested area shown in Fig. 3 are ratios expressed relative to their corresponding values in year 2000. The 2017 population data given by FAO are estimated based on the 2015 Revision of World Population Prospects from the United Nations Population Division.

Forestry inventory data of China. The forestry inventory data of China is provided by the State Forestry Administration of China (http://www.forestry.gov.cn). We used forest statistics documented in the National Continuous Forest Inventory of China (1999–2003 and 2009–2013) to calculate the afforested area, and the changes in forest area and coverage. We also used the planted forest map of China at a 1-km spatial resolution, which was obtained from the Seventh National Forest Resource Inventory (2004–2008).

Calculation of LAI trends. Trends in annual average MODIS LAI (2000 to 2017) and AVHRR LAI3gV1 (1982 to 2016 and 2000 to 2016) are evaluated by the Mann–Kendall test, which is a non-parametric test to detect monotonic trend in time series data. We used the function 'zyp.trend.vector' with the Yue–Pilon pre-whitening method provided by R package 'zyp' to conduct the trend test[57]. The trends with $P \leq 0.1$ are considered to be statistically significant in this study. Similar patterns are seen at $P \leq 0.05$ and the seven greening clusters (Fig. 1) are visible even at $P \leq 0.01$.

Calculation of the net change in leaf area. Trends in annual average MODIS LAI were considered to be linear when we calculated net changes in the leaf area during the period from 2000 to 2017. The net changes in leaf area for a specific region take into account the effects from both statistically significant browning and greening areas, and set the areas with statistically insignificant trends to a zero contribution, as shown in equation (1):

$$\text{Net leaf area changes per region} = \sum_{i=1}^{n} \mathrm{Tr}_i A_i N_{\mathrm{yr}} \quad (1)$$

where i represents a pixel with a statistically significant trend, n is the total number of such pixels in the region, Tr_i is the trend of a pixel, A_i is the area of a pixel that varies with latitudes, and N_{yr} is the length of the study period which is set to 17.

Growing season-integrated LAI and annual average LAI. The annual average LAI is used in our analyses, rather than a growing season-integrated LAI[7], as it is better suited for our global study, in which we aimed to emphasize the importance of land-use management, including different cropping cycles (single/multiple) and temporal changes. The annual average LAI has the advantage of being simple, can be evaluated for all regions of the globe, including those with multiple growing seasons, a year-long growing season in the tropical humid forests and when the growing season spans two calendar years. It does not suffer from certain limitations of growing season-integrated LAI, namely, the subjective use of thresholds to define the start and end dates of a growing season and interpolation of 16-day composite satellite data to a daily resolution[6].

Data availability

The datasets generated during and/or analysed in this study are publicly available as referenced within the article. All data and scripts are available from the corresponding author on request.

Received: 25 July 2018; Accepted: 2 January 2019;
Published online: 11 February 2019

References

1. Myneni, R. B. et al. Global products of vegetation leaf area and fraction absorbed PAR from year one of MODIS data. *Remote Sens. Environ.* **83**, 214–231 (2002).
2. Myneni, R. B., Keeling, C. D., Tucker, C. J., Asrar, G. & Nemani, R. R. Increased plant growth in the northern high latitudes from 1981 to 1991. *Nature* **386**, 698–702 (1997).
3. Zhou, L. et al. Variations in northern vegetation activity inferred from satellite data of vegetation index during 1981 to 1999. *J. Geophys. Res.* **106**, 20069–20083 (2001).
4. Xu, L. et al. Temperature and vegetation seasonality diminishment over northern lands. *Nat. Clim. Change* **3**, 581–586 (2013).
5. Vickers, H. et al. Changes in greening in the high Arctic: insights from a 30 year AVHRR max NDVI dataset for Svalbard. *Environ. Res. Lett.* **11**, 105004 (2016).
6. Park, T. et al. Changes in growing season duration and productivity of northern vegetation inferred from long-term remote sensing data. *Environ. Res. Lett.* **11**, 084001–084012 (2016).
7. Zhu, Z. et al. Greening of the Earth and its drivers. *Nat. Clim. Change* **6**, 791–795 (2016).
8. Piao, S. et al. Detection and attribution of vegetation greening trend in China over the last 30 years. *Glob. Change Biol.* **21**, 1601–1609 (2015).
9. Donohue, R. J., Roderick, M. L., McVicar, T. R. & Farquhar, G. D. Impact of CO_2 fertilization on maximum foliage cover across the globe's warm, arid environments. *Geophys. Res. Lett.* **40**, 3031–3035 (2013).
10. Keenan, T. F. et al. Recent pause in the growth rate of atmospheric CO_2 due to enhanced terrestrial carbon uptake. *Nat. Commun.* **7**, 13428 (2016).
11. Cheng, L. et al. Recent increases in terrestrial carbon uptake at little cost to the water cycle. *Nat. Commun.* **8**, 110 (2017).
12. Nemani, R. R. et al. Climate-driven increases in global terrestrial net primary production from 1982 to 1999. *Science* **300**, 1560–1563 (2003).
13. Goetz, S. J., Bunn, A. G., Fiske, G. J. & Houghton, R. A. Satellite-observed photosynthetic trends across boreal North America associated with climate and fire disturbance. *Proc. Natl Acad. Sci. USA* **102**, 13521–13525 (2005).
14. Fensholt, R. et al. Greenness in semi-arid areas across the globe 1981–2007 — an Earth Observing Satellite based analysis of trends and drivers. *Remote Sens. Environ.* **121**, 144–158 (2012).
15. Forkel, M. et al. Enhanced seasonal CO_2 exchange caused by amplified plant productivity in northern ecosystems. *Science* **351**, 696–699 (2016).
16. Mao, J. et al. Human-induced greening of the northern extratropical land surface. *Nat. Clim. Change* **6**, 959–963 (2016).
17. Bjorkman, A. D. et al. Plant functional trait change across a warming tundra biome. *Nature* **562**, 57–62 (2018).
18. Prestele, R. et al. Current challenges of implementing anthropogenic land-use and land-cover change in models contributing to climate change assessments. *Earth Syst. Dynam.* **8**, 369–386 (2017).
19. Piao, S. et al. Lower land-use emissions responsible for increased net land carbon sink during the slow warming period. *Nat. Geosci.* **11**, 739–743 (2018).
20. McMurtrie, R. E. et al. Why is plant-growth response to elevated CO_2 amplified when water is limiting, but reduced when nitrogen is limiting? A growth-optimisation hypothesis. *Funct. Plant Biol.* **35**, 521–534 (2008).
21. Wenzel, S., Cox, P. M., Eyring, V. & Friedlingstein, P. Projected land photosynthesis constrained by changes in the seasonal cycle of atmospheric CO_2. *Nature* **538**, 499–501 (2016).
22. Tian, F. et al. Evaluating temporal consistency of long-term global NDVI datasets for trend analysis. *Remote Sens. Environ.* **163**, 326–340 (2015).
23. Song, X. P. et al. Global land change from 1982 to 2016. *Nature* **560**, 639–643 (2018).
24. Yan, K. et al. Evaluation of MODIS LAI/FPAR product Collection 6. Part 1: consistency and improvements. *Remote Sens.* **8**, 359 (2016).
25. Yan, K. et al. Evaluation of MODIS LAI/FPAR product Collection 6. Part 2: validation and intercomparison. *Remote Sens.* **8**, 460 (2016).
26. Knyazikhin, Y., Martonchik, J. V., Myneni, R. B., Diner, D. J. & Running, S. W. Synergistic algorithm for estimating vegetation canopy leaf area index and fraction of absorbed photosynthetically active radiation from MODIS and MISR data. *J. Geophys. Res.* **103**, 32257–32275 (1998).
27. Zhu, Z. et al. Global data sets of vegetation leaf area index (LAI)3g and fraction of photosynthetically active radiation (FPAR)3g derived from global inventory modeling and mapping studies (GIMMS) normalized difference vegetation index (NDVI3g) for the period 1981 to 2011. *Remote Sens.* **5**, 927–948 (2013).
28. Wolf, J. et al. Biogenic carbon fluxes from global agricultural production and consumption. *Global Biogeochem. Cycles* **29**, 1617–1639 (2015).
29. Lobell, D. B., Schlenker, W. & Costa-Roberts, J. Climate trends and global crop production since 1980. *Science* **333**, 616–620 (2011).
30. Rosenzweig, C. & Parry, M. L. Potential impact of climate change on world food supply. *Nature* **367**, 133–138 (1994).
31. Jain, H. K. *Green Revolution: History, Impact and Future* (Studium, Houston, 2010).
32. Zeng, N. et al. Agricultural Green Revolution as a driver of increasing atmospheric CO_2 seasonal amplitude. *Nature* **515**, 394–397 (2014).
33. Buitenwerf, R., Sandel, B., Normand, S., Mimet, A. & Svenning, J.-C. Land surface greening suggests vigorous woody regrowth throughout European semi-natural vegetation. *Global Change Biol.* **24**, 5789–5801 (2018).
34. Fuchs, R., Herold, M., Verburg, P. H., Clevers, J. G. P. W. & Eberle, J. Gross changes in reconstructions of historic land cover/use for Europe between 1900 and 2010. *Global Change Biol.* **21**, 299–313 (2015).
35. Fuchs, R. et al. Assessing the influence of historic net and gross land changes on the carbon fluxes of Europe. *Global Change Biol.* **22**, 2526–2539 (2016).
36. Zhang, Y. et al. Multiple afforestation programs accelerate the greenness in the 'Three North' region of China from 1982 to 2013. *Ecol. Indic.* **61**, 404–412 (2016).
37. Zhang, Y., Yao, Y., Wang, X., Liu, Y. & Piao, S. Mapping spatial distribution of forest age in China. *Earth Space Sci.* **4**, 108–116 (2017).
38. Tong, X. et al. Increased vegetation growth and carbon stock in China karst via ecological engineering. *Nat. Sustain.* **1**, 44–50 (2018).
39. Peng, S. S. et al. Afforestation in China cools local land surface temperature. *Proc. Natl Acad. Sci. USA* **111**, 2915–2919 (2014).
40. Lu, F. et al. Effects of national ecological restoration projects on carbon sequestration in China from 2001 to 2010. *Proc. Natl Acad. Sci. USA* **115**, 4039–4044 (2018).
41. Feng, X. et al. Revegetation in China's Loess Plateau is approaching sustainable water resource limits. *Nat. Clim. Change* **6**, 1019–1022 (2016).
42. Chakraborty, A., Seshasai, M. V. R., Reddy, C. S. & Dadhwal, V. K. Persistent negative changes in seasonal greenness over different forest types of India using MODIS time series NDVI data (2001–2014). *Ecol. Indic.* **85**, 887–903 (2018).
43. Zhang, Y., Song, C., Band, L. E., Sun, G. & Li, J. Reanalysis of global terrestrial vegetation trends from MODIS products: browning or greening? *Remote Sens. Environ.* **191**, 145–155 (2017).
44. *FAOSTAT Database* (FAO, 2018); http://www.fao.org/faostat/
45. Ray, D. K. & Foley, J. A. Increasing global crop harvest frequency: recent trends and future directions. *Environ. Res. Lett.* **8**, 044041 (2013).
46. Lu, C. & Tian, H. Global nitrogen and phosphorus fertilizer use for agriculture production in the past half century: shifted hot spots and nutrient imbalance. *Earth Syst. Sci. Data* **9**, 181–192 (2017).
47. Mueller, N. D. et al. Closing yield gaps through nutrient and water management. *Nature* **490**, 254–257 (2012).
48. Ambika, A. K., Wardlow, B. & Mishra, V. Remotely sensed high resolution irrigated area mapping in India for 2000 to 2015. *Sci. Data* **3**, 160118 (2016).
49. Myneni, R., Knyazikhin Y. & Park, T. *MOD15A2H MODIS/Terra Leaf Area Index/FPAR 8-day L4 Global 500 m SIN Grid V006 Data Set* (NASA, 2015); https://doi.org/10.5067/MODIS/MOD15A2H.006
50. Myneni, R., Knyazikhin, Y. & Park, T. *MYD15A2H MODIS/Aqua Leaf Area Index/FPAR 8-day L4 Global 500 m SIN Grid V006 Data Set* (NASA, 2015); https://doi.org/10.5067/MODIS/MYD15A2H.006
51. Samanta, A. et al. Comment on "Drought-induced reduction in global terrestrial net primary production from 2000 through 2009". *Science* **333**, 1093 (2011).
52. MODIS land team. *Validation: Status for LAI/FPAR (MOD15)* (NASA, 2018); https://landval.gsfc.nasa.gov/ProductStatus.php?ProductID=MOD15
53. Pinzon, J. & Tucker, C. A non-stationary 1981–2012 AVHRR NDVI3g time series. *Remote Sens.* **6**, 6929–6960 (2014).
54. Friedl, M. A., McIver, D. K., Hodges, J. & Zhang, X. Y. Global land cover mapping from MODIS: algorithms and early results. *Remote Sens. Environ.* **83**, 287–302 (2002).
55. Dimiceli, C. et al. *MOD44B MODIS/Terra Vegetation Continuous Fields Yearly L3 Global 250 m SIN Grid V006 Data Set* (NASA, 2015); https://doi.org/10.5067/MODIS/MOD44B.006
56. Harris, I. C. & Jones, P. D. *CRU TS4.01: Climatic Research Unit (CRU) Time-Series (TS) version 4.01 of High-Resolution Gridded Data of Month-by-Month Variation in Climate (Jan. 1901–Dec. 2016)* (Centre for Environmental Data Analysis, 2017); https://doi.org/10.5285/58a8802721c94c66ae45c3baa4d814d0
57. Bronaugh, D. & Werner, A. zyp: Zhang + Yue-Pilon trends package. R package version 0.10-1 https://cran.r-project.org/web/packages/zyp/index.html (2013).

Acknowledgements

This work was funded by NASA Earth Science Directorate. R.B.M. acknowledges funding by the Alexander von Humboldt Foundation. T.P. was funded by the NASA Earth and Space Science Fellowship Program. P.C. was funded by the French Agence Nationale de la Recherche (ANR) Convergence Lab Changement climatique et usage des terres (CLAND) and by the European Research Council Synergy project SyG-2013-610028 IMBALANCE-P. H.T. was funded by the Research Council of Norway

(RCN #287402) and Nordforsk (CLINF). The article-processing charges for this publication were paid for by funds from a NASA Research Grant to Boston University.

Author Contributions

C.C. carried out the analyses with contributions from T.P., X.W., B.X., R.K.C. and R.F. C.C. and R.B.M. wrote the article. All authors contributed ideas for analyses, comments and critiques on drafts.

Competing interests

The authors declare no competing interests.

Additional information

Supplementary information is available for this paper at https://doi.org/10.1038/s41893-019-0220-7.

Reprints and permissions information is available at www.nature.com/reprints.

Correspondence and requests for materials should be addressed to C.C.

Publisher's note: Springer Nature remains neutral with regard to jurisdictional claims in published maps and institutional affiliations.

Characteristics, drivers and feedbacks of global greening

Shilong Piao[1,2,3]*, *Xuhui Wang*[1], *Taejin Park*[4,5], *Chi Chen*[4], *Xu Lian*[1], *Yue He*[1], *Jarle W. Bjerke*[6], *Anping Chen*[7], *Philippe Ciais*[1,8], *Hans Tømmervik*[6], *Ramakrishna R. Nemani*[5] *and Ranga B. Myneni*[4]

Abstract | Vegetation greenness has been increasing globally since at least 1981, when satellite technology enabled large-scale vegetation monitoring. The greening phenomenon, together with warming, sea-level rise and sea-ice decline, represents highly credible evidence of anthropogenic climate change. In this Review, we examine the detection of the greening signal, its causes and its consequences. Greening is pronounced over intensively farmed or afforested areas, such as in China and India, reflecting human activities. However, strong greening also occurs in biomes with low human footprint, such as the Arctic, where global change drivers play a dominant role. Vegetation models suggest that CO_2 fertilization is the main driver of greening on the global scale, with other factors being notable at the regional scale. Modelling indicates that greening could mitigate global warming by increasing the carbon sink on land and altering biogeophysical processes, mainly evaporative cooling. Coupling high temporal and fine spatial resolution remote-sensing observations with ground measurements, increasing sampling in the tropics and Arctic, and modelling Earth systems in more detail will further our insights into the greening of Earth.

Afforestation
The conversion of treeless lands to forests through planting trees.

Vegetation controls the exchange of carbon, water, momentum and energy between the land and the atmosphere, and provides food, fibre, fuel and other valuable ecosystem services[1,2]. Changes in vegetation structure and function are driven by climatic and environmental changes, and by human activities such as land-use change. Given that increased carbon storage in vegetation, such as through afforestation, could combat climate change[3,4], quantifying vegetation change and its impact on carbon storage and climate has elicited considerable interest from scientists and policymakers.

However, it is not possible to detect vegetation changes at the global scale using ground-based observations due to the heterogeneity of change and the lack of observations that can detect these changes both spatially and temporally. While monitoring the changes in some vegetation properties (for example, stem-size distribution and below-ground biomass) at the global scale remains impossible, satellite-based remote sensing has enabled continuous estimation of a few important metrics, including vegetation greenness, since the 1980s (BOX 1).

In 1986, a pioneering study by Tucker et al.[5] on remotely sensed normalized difference vegetation index (NDVI; a radiometric measure of vegetation greenness) (BOX 1) revealed a close connection between vegetation canopy greenness and photosynthesis activity (as inferred from seasonal variations in atmospheric CO_2 concentration). This index was successfully used to constrain vegetation primary production globally[6]. Using NDVI data from 1981 to 1991, Myneni et al.[7] reported an increasing trend in vegetation greenness in the Northern Hemisphere, which was subsequently observed across the globe[8–13]. This 'vegetation greening' is defined as a statistically significant increase in annual or seasonal vegetation greenness at a location resulting, for instance, from increases in average leaf size, leaf number per plant, plant density, species composition, duration of green-leaf presence due to changes in the growing season and increases in the number of crops grown per year.

There has also been considerable interest in understanding the mechanisms or drivers of greening[11,14]. Lucht et al.[14] and Xu et al.[10] revealed that warming has eased climatic constraints, facilitating increasing vegetation greenness over the high latitudes. Zhu et al.[11] further investigated key drivers of greenness trends and concluded that CO_2 fertilization is a major factor driving vegetation greening at the global scale. Subsequent studies based on fine-resolution and medium-resolution satellite data[13] have shown the critical role of land-surface history, including afforestation and agricultural intensification, in enhancing vegetation greenness. The large spatial scale of vegetation greening and the robustness of its signal have led the Intergovernmental Panel on Climate Change (IPCC) special report on climate change

*e-mail: slpiao@pku.edu.cn

https://doi.org/10.1038/s43017-019-0001-x

Key points

- Long-term satellite records reveal a significant global greening of vegetated areas since the 1980s, which recent data suggest has continued past 2010.
- Pronounced greening is observed in China and India due to afforestation and agricultural intensification.
- Global vegetation models suggest that CO_2 fertilization is the main driver of global vegetation greening.
- Warming is the major cause of greening in boreal and Arctic biomes, but has negative effects on greening in the tropics.
- Greening was found to mitigate global warming through enhanced land carbon uptake and evaporative cooling, but might also lead to decreased albedo that could potentially cause local warming.
- Greening enhances transpiration, a process that reduces soil moisture and runoff locally, but can either amplify or reduce runoff and soil moisture regionally through altering the pattern of precipitation.

and land[15] to list it, together with global-scale warming, sea-level rise[16] and sea-ice decline[16], as highly credible evidence of the environmental impact of anthropogenic climate change.

Greener vegetation not only results from climatic and atmospheric changes but also feeds back to the climate through biogeochemical and biogeophysical processes. These feedbacks are often studied with Earth system models (ESMs), in which vegetation is coupled with the atmosphere and the hydrologic cycle[17]. ESM-based studies have demonstrated that greening can accelerate the hydrologic cycle by increasing the amount of water transpired by plants, alter the energy exchange between land and the atmosphere, and affect atmospheric circulation patterns[18,19].

In this Review, we synthesize past and recent efforts to characterize the spatiotemporal patterns of vegetation greening since the 1980s. We discuss how rising atmospheric CO_2 concentration, climate change, land-use change and nitrogen deposition are the key drivers of greenness changes on the global and regional scale. We assess the impacts of vegetation greening on carbon, water and energy balances, and conclude by identifying key challenges and perspectives for future research.

Greenness changes

Global-scale vegetation greening has been demonstrated using nearly four decades of NDVI and leaf area index (LAI) greenness data derived from the Advanced Very-High-Resolution Radiometer (AVHRR) instrument (FIG. 1a,b). While early studies primarily used the NDVI to detect changes in global greenness, recent studies widely use the LAI, since it has clear physical interpretation and is a fundamental variable in almost all land-surface models (BOX 1). An ensemble of LAI datasets has shown that 52% ($P<0.05$) to 59% ($P<0.10$) of global vegetated lands displayed an increasing trend in growing season LAI since the 1980s[11] (FIG. 1a). Although some studies reported a stalling, or even a reversal, of the greening trend since 2000 based on AVHRR[20] and collection 5 (C5) of the Moderate Resolution Imaging Spectroradiometer (MODIS) data[21], this signal might be an artefact of sensor degradation and/or processing[22–24]. For example, using a revised calibration of the MODIS data in the most recent collection 6 (C6) dataset[24], Chen et al.[13] showed that leaf area increased by 5.4 million km^2 over 2000–2017, an area equivalent to the areal extent of the Amazon rainforest[13]. Indeed, 34% of vegetated land exhibited greening ($P<0.10$), whereas only 5% experienced browning ($P<0.10$), that is, a loss of vegetation greening.

New satellite-based vegetation indices also support the global greening trend observed since 2000 (FIG. 1), including the enhanced vegetation index (EVI) and near-infrared reflectance of terrestrial vegetation (NIRv) (BOX 1). However, while vegetation greenness is increasing at the global scale, the changes vary considerably between regions and seasons.

Regional trends. In the high northern latitudes (>50°N), AVHRR and Landsat records indicate a widespread increase in vegetation greenness since the 1980s[8,12,25] (FIG. 2a–d). Regions with the greatest greening trend include northern Alaska and Canada, the low-Arctic parts of eastern Canada and Siberia, and regions of Scandinavia[12,25,26]. Dendrochronological data and photographic evidence further corroborate these findings[27–30]. In general, the LAI over high northern latitudes will continue to increase by the end of this century[31], based on the results of an ensemble of ESMs (FIG. 2e–h). However, although only 3% of the high latitudes show browning during 1982–2014 (REF.[25]), there is a growing proportion of Arctic areas exhibiting a browning trend[32]. Such trends first emerged in boreal forests, where a multitude of disturbances (for example, fires, harvesting and insect defoliation) prevail[9,33–37]. The North American boreal forests in particular exhibit browning areas nearly 20 times larger than the Eurasian boreal forests, showing heterogeneous regional greenness change[38].

The northern temperate region (25–50°N) is another vegetation greening hotspot, experiencing faster rates of greening than the high latitudes since 2000 (FIG. 2b,d). Indeed, ~14 million km^2 of the temperate region greened ($P<0.10$), contributing about one-half of the global net leaf area increase over this time period[13]. The increase of vegetation greenness is especially strong in agricultural regions (for example, India[13]) and recently afforested areas (for example, China[13,39]); collectively, China and India alone contribute more than 30% of the total net increase in the global LAI[13].

Tropical regions (25°S–25°N) are also greening (FIG. 2b,d), contributing about a quarter of the net global

Author addresses

[1]Sino-French Institute for Earth System Science, College of Urban and Environmental Sciences, Peking University, Beijing, China.
[2]Key Laboratory of Alpine Ecology, Institute of Tibetan Plateau Research, Chinese Academy of Sciences, Beijing, China.
[3]Center for Excellence in Tibetan Earth Science, Chinese Academy of Sciences, Beijing, China.
[4]Department of Earth and Environment, Boston University, Boston, MA, USA.
[5]NASA Ames Research Center, Moffett Field, CA, USA.
[6]Norwegian Institute for Nature Research, FRAM – High North Research Centre for Climate and the Environment, Tromsø, Norway.
[7]Department of Biology, Colorado State University, Fort Collins, CO, USA.
[8]Laboratoire des Sciences du Climat et de l'Environnement, CEA CNRS UVSQ, Gif-sur-Yvette, France.

Box 1 | **Remotely sensed vegetation greenness**

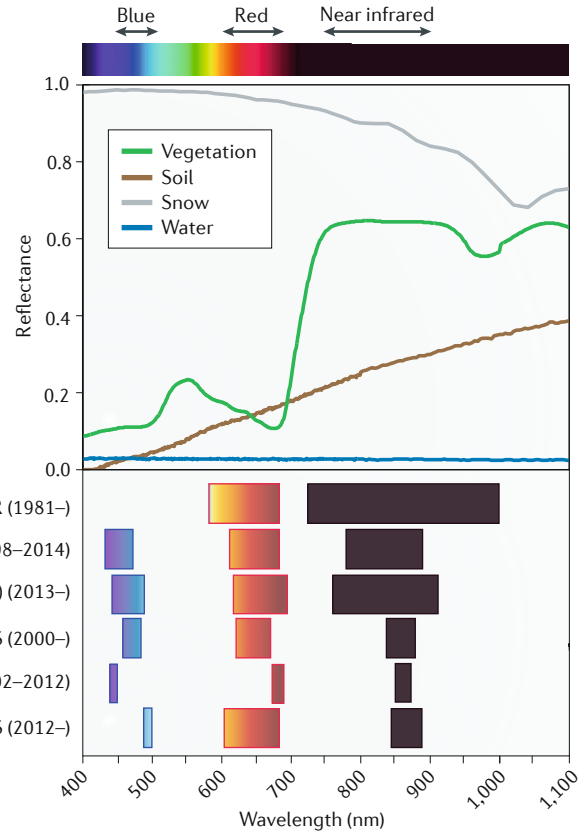

Remotely sensed vegetation greenness generally refers to spectral vegetation indices (VIs) or the leaf area index (LAI). Photosynthetic pigments in plant leaves (mainly chlorophyll and carotenoids) strongly absorb photosynthetically active radiation, which largely overlaps with the visible spectrum (400–700 nm), particularly red wavelengths (620–700 nm). In the near-infrared (NIR) domain (700–1,300 nm), absorbance by leaf constituents is either small or absent; thus, scattering increases the likelihood that photons will exit the leaf. This is the biophysical basis for high leaf-level reflectance in the NIR region. At the canopy scale, structural properties such as LAI and leaf-angle distribution dominate variability in NIR reflectance[176]. This unique spectral signature of vegetation in the red and NIR channels, a characteristic not present in common non-vegetative features such as soil, snow and water[177,178], has thus been utilized to derive numerical VIs measuring vegetation greenness[176,179,180] (Supplementary Table S1). For example, the normalized difference vegetation index, which is one of the most widely used VIs in assessing vegetation greenness and its changes from local to global scales (Supplementary Table S2), is useful for measuring canopy structural properties, such as leaf area, light interception and biomass[41,181,182]. Satellite sensors, such as the Advanced Very-High-Resolution Radiometer (AVHRR), Moderate Resolution Imaging Spectroradiometer (MODIS), Vegetation, Medium Resolution Imaging Spectrometer (MERIS) and Visible Infrared Imaging Radiometer Suite (VIIRS), have been deployed with varying temporal coverage, providing VI products based on a wide range of spectral-band specifications and data processing (Supplementary Table S3). For example, the AVHRR does not have a blue channel, so this sensor is unable to produce blue-band-based greenness indices like the enhanced vegetation index. These sensor differences make it a non-trivial challenge to produce consistent and continuing long-term greenness products[183].

Compared with VIs, the LAI (the one-sided green leaf area per unit ground area in broadleaf canopies or one-half of the total needle surface area per unit ground area in coniferous canopies[184,185]) is a well-defined physical attribute of vegetation. The LAI is a state variable in all land models and key to quantifying the exchanges of mass, momentum and energy between the surface and the atmosphere. Multiple approaches for retrieving the LAI from remote sensing data have been developed — these can be conceptually categorized as: empirical approaches that are based on relationships between VIs and the LAI[186,187]; machine-learning approaches that train surface reflectance or VIs to given reference LAIs[182,188,189]; and physical approaches that are based on the physics of radiation interaction with elements of a canopy and transport within the vegetative medium[184,190,191]. See Supplementary Table S4 for currently available global LAI products.

increase in leaf area since 2000 (REF.[13]). However, the tropics also have areas where significant browning has been reported, for example, in the Brazilian Cerrado and Caatinga regions and Congolian forests[13,40]. It is worth noting that substantial uncertainties remain in the tropical vegetation greenness estimations due to the saturation effects of greenness indices in dense vegetation[41] and contamination by clouds and aerosols[42]. These uncertainties partly underlie the disagreement between the MODIS and AVHRR products[13] when measuring tropical greenness and the debate on whether the Amazonian forests have greened or browned in response to droughts[42–44].

The extratropical Southern Hemisphere (>25°S) has experienced a general greening trend since the 1980s[13,45], but it is lower than that in the temperate and high-latitude Northern Hemisphere[13] (FIG. 2a–d). Regional greening hotspots in southern Brazil and southeast Australia mostly overlap with the intensive cropping areas[13], highlighting the increasing contribution of managed ecosystems to vegetation greening. Note that most of this region is dominated by semi-arid ecosystems[46], where vegetation coverage is generally sparse. Thus, satellite vegetation indices over this region are generally sensitive to change in soil background. For example, browning was detected from the AVHRR dataset since the 2000s[20] (FIG. 2b), but MODIS C6 data (which is better calibrated and can distinguish vegetation from background more accurately) instead showed an overall greening trend particularly since 2002 (REF.[13]; FIG. 2c,d).

Land-surface phenology
Cyclic phenomena in vegetated land surfaces observed from remote sensing.

Seasonal changes of greenness. In the northern temperate and high latitudes, greenness often shows distinctive seasonal patterns within a calendar year (FIG. 3). Several metrics of land-surface phenology have been developed

Carboxylation
The addition of CO_2 to ribulose 1,5-bisphosphate during photosynthesis.

to depict the seasonal cycle of greenness[47], including the widely used start of the growing season (SOS) and end of the growing season (EOS)[48]. Although phenology dates can vary depending on the greenness product or algorithm used[49–51], significant trends towards both earlier SOS (2–8 days decade^{-1}) and later EOS (1–6 days decade^{-1}) and, thus, longer lengths of the growing season (LOS) (2–10 days decade^{-1}), have been observed in most Northern Hemisphere regions during the past four decades[7,8,25,52–54] (FIG. 3a–c). These trends are corroborated by ground-based observation data in spring and autumn[55–57]. The increase in LOS is driven mainly by an advanced SOS in Eurasia (53–81% of LOS lengthening is due to SOS advance) and delayed EOS in North America (57–96% of LOS lengthening is due to EOS delay), with the more rapid total LOS increase seen in Eurasia[25,58–60].

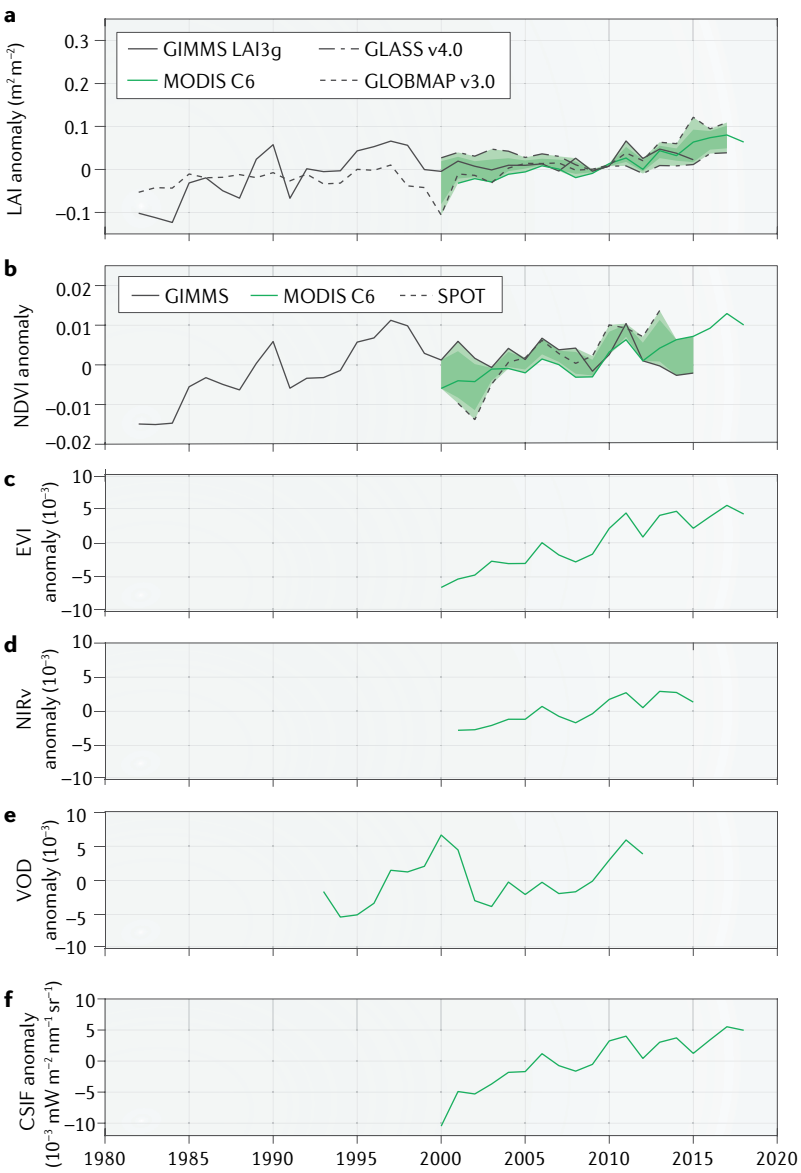

Fig. 1 | **Changes in satellite-derived global vegetation indices, vegetation optical depth and contiguous solar-induced fluorescence. a** | Leaf area index (LAI) from four products: GIMMS[13], GLASS[192], GLOBMAP[23] and Moderate Resolution Imaging Spectroradiometer (MODIS) C6 (REF.[193]). **b** | Normalized difference vegetation index (NDVI) from three products: GIMMS[194], MODIS C6 (REF.[195]) and SPOT[196]. **c** | Enhanced vegetation index (EVI) from MODIS C6 (REF.[195]). **d** | Near-infrared reflectance of terrestrial vegetation (NIRv)[197]. **e** | Vegetation optical depth (VOD)[119]. **f** | Contiguous solar-induced fluorescence (CSIF)[114]. In parts **a** and **b**, the light-green shading denotes the range of LAI and NDVI across different products and the dark-green shading denotes the interquartile range (between the 25th and 75th percentiles). Only measurements during the growing season[11] were considered.

In addition to longer growing seasons, satellite greenness data also reveal important shifts in the timing and magnitude of the seasonal peak greenness[47,61]. For example, the timing of peak greenness has advanced by 1.2 days decade^{-1} during 1982–2015 (REF.[62]) and 1.7 days decade^{-1} during 2000–2016 (REF.[61]) over the extratropical Northern Hemisphere (FIG. 3a), with the boreal region peak greenness advancing twice as fast as the Arctic tundra and temperate ecosystem peaks[61]. Since the 1980s, the magnitude of the peak greenness has also increased over the extratropical Northern Hemisphere by ~0.1 standardized NDVI anomaly per year[62], with a stronger signal in the pan-Arctic region[63,64].

Phenology changes, including the SOS advancement, EOS delay and peak greenness enhancement, can significantly change the Earth's seasonal landscape. Northern high latitudes, which traditionally have high seasonality (that is, short and intense growing seasons), are exhibiting seasonality similar to that of their counterparts 6° to 7° south in the 1980s. In other words, the latitudinal isolines of northern vegetation seasonality have shifted southward since the 1980s. The diminished seasonality of the northern high-latitude vegetation[10] is consistent with changes in the velocity of vegetation greenness (defined as the ratio of temporal greenness change to its spatial gradient)[65], which showed faster northward movement of the SOS (3.6 ± 1.0 km year^{-1}) and the EOS (6.0 ± 1.1 km year^{-1}) than the peak greenness (3.1 ± 1.0 km year^{-1}) during 1982–2011 (REF.[65]).

Drivers of greening

Several factors are thought to impact vegetation greening, including rising atmospheric CO_2 concentrations, climate change, nitrogen deposition and land-use changes. However, nonlinear impacts and interactions make it challenging to quantify the individual contribution of these factors to the observed greening trend. In this section, we review the contribution of several key drivers of vegetation greening and efforts to quantitatively attribute the observed greening trend to each of these factors.

CO_2 fertilization. As CO_2 is the substrate for photosynthesis, rising atmospheric CO_2 concentration can enhance photosynthesis[66] by accelerating the rate of carboxylation; this process is known as the 'CO_2 fertilization effect'. In addition, increased CO_2 concentrations can also enhance vegetation greenness by partially closing leaf stomata, leading to enhanced water-use efficiency[67], which should relax water limitation to plant growth, particularly over semi-arid regions[45,68,69]. Analysis of the 'Trends and drivers of the regional-scale sources and sinks of carbon dioxide' (TRENDY) ensemble of dynamic global vegetation models (DGVMs)[70] suggests that rising CO_2 is the dominant driver of vegetation greening, accounting for nearly 70% of global

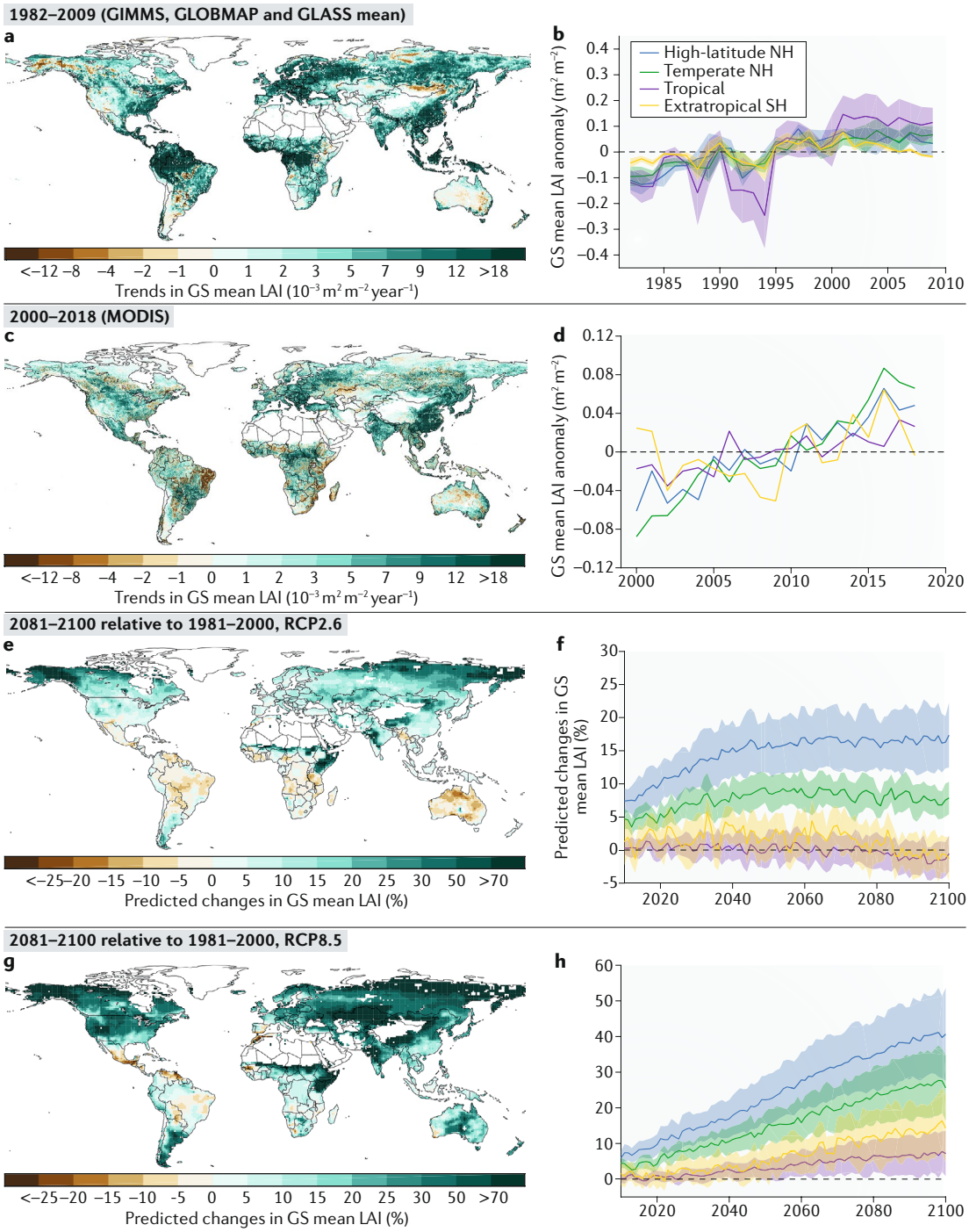

Fig. 2 | **Spatial patterns of changes in leaf area index. a** | Growing season (GS) mean Advanced Very-High-Resolution Radiometer (AVHRR) leaf area index (LAI) trend during 1982–2009. The AVHRR LAI dataset is the average of three different products (GIMMS[13], GLOBMAP[23] and GLASS[192]). **b** | Change in the GS mean AVHRR LAI over four regions during 1982–2009. **c** | GS mean Moderate Resolution Imaging Spectroradiometer (MODIS) LAI during 2000–2018. **d** | Change in the GS mean MODIS LAI over four regions during 2000–2018. MODIS LAI is from collection 6 (REF.[193]). **e** | Relative change in GS mean LAI between 1981–2000 and 2081–2100 under the Representative Concentration Pathway 2.6 (RCP2.6), based on the Coupled Model Intercomparison Project Phase 5 (CMIP5) multi-model ensemble. **f** | Relative change in GS mean CMIP5 LAI 2018–2100 under RCP2.6, relative to 1981–2000. **g** | Relative change in GS mean LAI between 1981–2000 and 2081–2100 under RCP8.5, based on CMIP5. **h** | Relative change in GS mean CMIP5 LAI 2018–2100 under RCP8.5, relative to 1981–2000. The number of CMIP5 models used in the calculation of the multi-model mean is 16 and 19, for RCP2.6 and RCP8.5, respectively (Supplementary Table S5). In parts **a**, **c**, **e** and **g**, the white land areas depict barren lands, permanent ice-covered areas, permanent wetlands, built-up areas and water. In parts **b**, **d**, **f** and **h**, blue represents the high-latitude Northern Hemisphere (NH) (50–90°N), green represents the temperate NH (25–50°N), purple represents the tropical zone (25°S–25°N) and yellow represents the extratropical Southern Hemisphere (SH) (90–25°S). The shading shows the ±1 inter-model standard deviation.

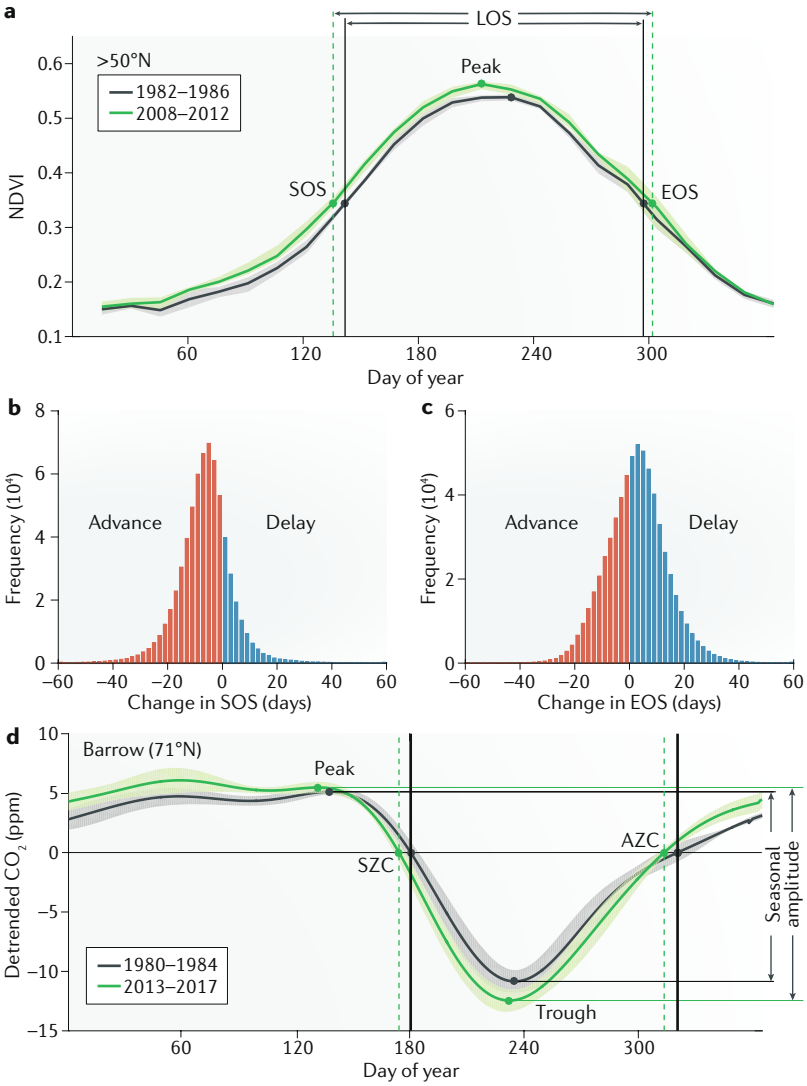

Fig. 3 | **Changes in the seasonality of vegetation greenness and atmospheric CO_2 concentration. a** | Five-year mean seasonal variations of the normalized difference vegetation index (NDVI) over Northern Hemisphere high latitudes (>50°N) during 1982–1986 (black line) and 2008–2012 (green line). Start of the growing season (SOS) and end of the growing season (EOS) are shown as 50% of the maximum NDVI. The length of the growing season (LOS) is the difference between the EOS and the SOS. **b** | Frequency distribution of SOS change in the Northern Hemisphere during 1982–2012. **c** | Frequency distribution of EOS change in the Northern Hemisphere during 1982–2012. **d** | Five-year mean detrended seasonal CO_2 variations at Barrow, AK, USA (71°N) (NOAA ESRL archive: https://www.esrl.noaa.gov/gmd/ccgg/obspack/) during 1980–1984 (black line) and 2013–2017 (green line). Vertical lines mark the spring zero-crossing date (SZC) and autumn zero-crossing date (AZC). Horizontal lines mark the seasonal amplitude as the difference between the maximum and the minimum of detrended seasonal CO_2 variations. Shaded areas show the range of interannual variations in the NDVI in part **a** and the standard deviation of the detrended CO_2 mole fraction (ppm) in part **d** at the day of year. NDVI data are the updated dataset from Tucker et al.[194]. Parts **b** and **c** are adapted with permission from REF.[48], Wiley-VCH.

LAI trend since the 1980s[11] (FIG. 4). Statistical modelling also supports the important role of rising atmospheric CO_2 concentration in driving vegetation greening[71,72]. Free-air CO_2 enrichment (FACE) experiments show that elevating the CO_2 concentration by ~200 ppm above the ambient conditions significantly enhances vegetation productivity[73] and increases leaf area[74]. Different plant species vary largely in the magnitude of LAI enhancement[75], with the larger effect on forest stands having lower LAI at the ambient conditions[76]. In DGVMs, elevated CO_2 increases vegetation productivity more in tropical ecosystems than in temperate and boreal ecosystems[11,77,78] (FIG. 4b). However, the strength of the CO_2 fertilization effect can be limited by extreme weather events[79,80] and nutrient and water availability[73,81,82]. Indeed, nitrogen and phosphorus have been shown to regulate the global pattern of CO_2 fertilization effects[83]. Since nutrient processes were under-represented in the ESMs used in the IPCC Fifth Assessment Report (AR5), the predictions of continued greening trends through 2100 (REF.[31]) (FIGS 2e–h,5) might overestimate the CO_2 fertilization effects.

Climate change. Although rising atmospheric CO_2 concentration is the main driver of global greening, climate change, such as anthropogenic warming and regional trends in precipitation, is a dominant driver of greenness changes over 28% of the global vegetated area[11]. The global contribution of climate change to increasing greenness is only 8% (FIG. 4a), however, because impacts of climate change on vegetation greenness vary between regions[11]. For example, warming could reduce vegetation growth in the tropics[84], where ambient temperature is close to vegetation optimal temperature[85], but warming significantly increases vegetation greenness in the boreal and Arctic regions[86] by enhancing metabolism[87] and extending the growing season[59,88,89]. DGVM simulations show that the positive effects of climate change, primarily from warmer temperature[14], dominate the greening trend over more than 55% of the northern high latitudes (FIG. 4b) and in the Tibetan Plateau[11]. However, this positive impact of anthropogenic warming on greenness appears to have weakened during the past four decades[90,91], when the correlation coefficient between temperature and greenness decreased by more than 50%[90,91], suggesting a possible saturation of future greening in response to warmer temperature.

In water-limited ecosystems, changes in precipitation — reflecting either decadal climate variability or trends from anthropogenic climate change — were suggested as the main driving factor of greening and browning[45,92]. Precipitation-driven greening is most evident in the African Sahel[93,94] and semi-arid ecosystems of southern Africa and Australia[45,95] (FIG. 4c). Both empirical models and DGVMs indicate that 'the greening Sahel', one of the early examples of vegetation greening detected by satellite measurements[93,94], was primarily driven by increases in precipitation after a severe drought in the early 1980s[96–98]. This causal relationship between precipitation and greenness changes was further supported through analyses of recent microwave satellite measurements and long-term field surveys[99,100].

Land-use change. Like climate change, land-use change exerts a considerable but highly spatially variable influence on greenness changes[11,13] (FIG. 4). Specifically, deforestation dominates the tropics[101,102], while afforestation increases forest area over temperate regions,

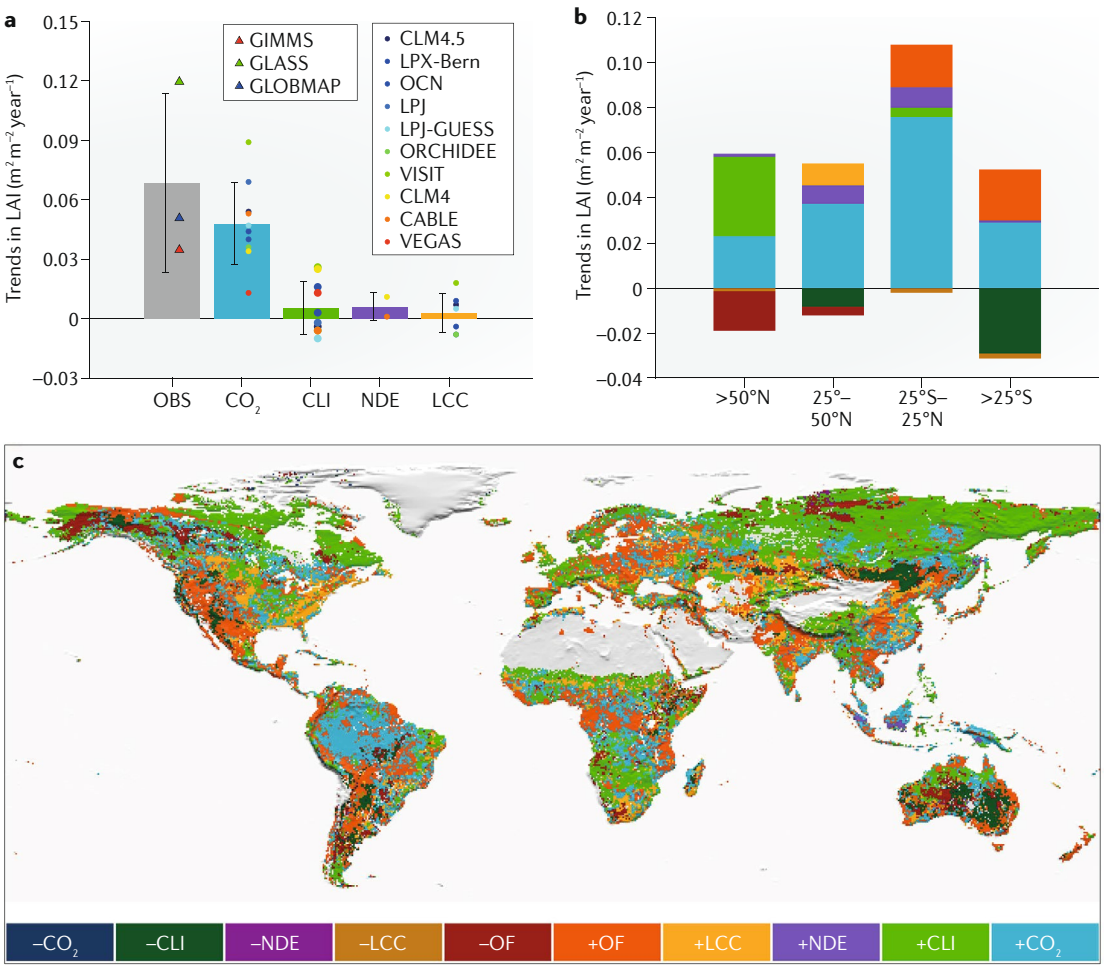

Fig. 4 | **Attribution of trends in growing season mean leaf area index. a** | Trends in the global-averaged leaf area index (LAI) derived from satellite observation (OBS) and attributed respectively to rising CO_2 (CO_2), climate change (CLI), nitrogen deposition (NDE) and land cover change (LCC) during 1982–2009 (REF.[11]). The error bars show the standard deviation of trends derived from satellite data and model simulations. Individual model-estimated contributions of each driver to LAI trends are shown as coloured dots. **b** | Contribution of different drivers to LAI change in latitude bands (>50°N, 25–50°N, 25°S–25°N, >25°S). **c** | Spatial distribution of the dominant driver of growing season mean LAI trend, defined as the driver that contributes the most to the increase (or decrease) in LAI in each vegetated grid cell. Other factors (OF) is defined by the fraction of the observed LAI trends not accounted for by modelled factors. Parts **b** and **c** share the same colour legend, where the '+' prefix indicates a positive effect from the corresponding driver on LAI trends and the '−' prefix indicates a negative effect. Data courtesy of Zhu et al.[11]. Part **c** adapted from REF.[11], Springer Nature Limited.

particularly in China, where the forest area has increased by more than 20% since the 1980s[103]. The TRENDY ensemble of DGVMs[70] indicates that greenness changes over 19% of the northern temperate vegetation (25–50°N) are primarily driven by land-use change[11] (FIG. 4c). However, this might be an underestimate since critical land-use processes[104,105] are under-represented or missing in the current generation of DGVMs. For example, forest-age dynamics are not represented in most DGVMs, even though one-third of the global forests are younger than 20 years old[106], implying that forest regrowth might contribute to global greening in the future. In addition, agricultural intensification with multiple cropping, irrigation and fertilizer usage must contribute considerably to vegetation greening, which is exemplified by the dominance of other unmodelled factors over agricultural lands of India, China and Eastern Europe (FIG. 4c).

Nitrogen deposition. Anthropogenic changes in the amount, rate and distribution of nitrogen deposition can impact greening patterns, since insufficient nitrogen availability can stunt plant growth[107–109], potentially slowing greening or causing browning, but excess nitrogen can enhance plant growth in nitrogen-limited systems[109]. However, the few DGVMs that include the nitrogen cycle do not indicate that nitrogen deposition plays a dominant driving role on the greening at either the global or regional scales (FIG. 4). Modelling studies differ on the contribution of increasing nitrogen deposition to the global LAI increase[11] (9 ± 12%), largely due to the incomplete representation of nitrogen-related processes[110]. A growing number of DGVMs are currently incorporating nitrogen processes[111], though, and future research priorities include better measurement and representation of processes such as plant nitrogen uptake and allocation[110].

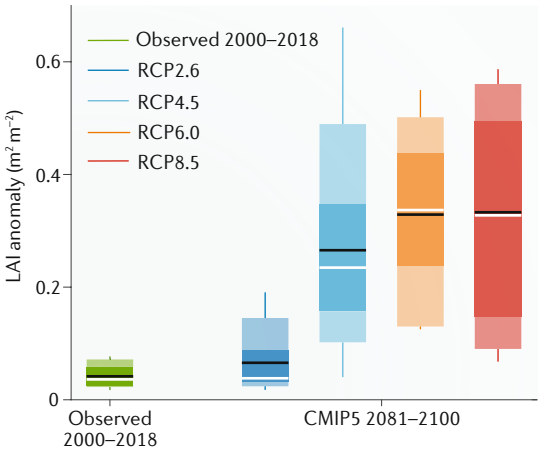

Fig. 5 | **Current and predicted global leaf area index.** Current (observed 2000–2018) leaf area index (LAI) anomaly ($m^2 m^{-2}$) from an average of satellite measurements based on GIMMS[13], GLASS[192], GLOBMAP[23] and Moderate Resolution Imaging Spectroradiometer (MODIS) C6 (REF.[193]). Predicted LAI anomalies from the Coupled Model Intercomparison Project Phase 5 (CMIP5) multi-model (Supplementary Table S5) projections during 2081–2100. The boxes and whiskers indicate the minimum, 10th, 25th, 50th, 75th and 90th percentiles and the maximum LAI of CMIP5 models; the black and white lines indicate the mean and median LAI of CMIP5 models, respectively. LAI anomalies were calculated against the average during 1980–2005.

Impact of greening on the carbon cycle

Greening increases the amount of photosynthetically active sunlight that is absorbed by vegetation and, thus, enhances productivity[112,113]. There has been substantial evidence showing enhanced vegetation productivity from contiguous solar-induced fluorescence (CSIF; FIG. 1f) observations[114], empirical models of vegetation productivity[92,115] and DGVM and ESM simulations[70,116] (FIG. 6). It should be noted, though, that CSIF is not fully independent from MODIS greenness indices, since its derivation relies on both solar-induced fluorescence measurements from Orbiting Carbon Observatory 2 and MODIS reflectance measurements[114].

Enhanced vegetation productivity increases terrestrial carbon storage, slowing down anthropogenic climate warming[117]. For example, about 29% of anthropogenic CO_2 emissions since the 1980s have been offset by the land carbon sink (2.5 ± 1.0 PgC $year^{-1}$)[111]. This vegetation-induced large land carbon sink was also inferred from forest inventories[118] and above-ground biomass estimated from the vegetation optical depth (FIG. 1e), a microwave-based satellite measurement of both woody and leaf biomass[119]. Multiple lines of evidence, including analyses from DGVMs, atmospheric inversion models and the residual land sink (the mass balance residual of anthropogenic CO_2 emissions, atmospheric CO_2 growth rate and ocean CO_2 budget), confirm the increasing magnitude of the global land carbon sink since the 1980s[111] (FIG. 6). An ecosystem model driven by satellite LAI measurements estimated that increased LAI accounts for 36% (0.4 PgC $year^{-1}$) of the land carbon sink enhancement of 1981–2016 (REF.[112]). Recent studies indicate that the trend in the land carbon sink has further accelerated since the late 1990s[120,121]. For example, the rate of update during 1998–2012 was three times that of 1980–1988 (0.17 PgC $year^{-2}$ in comparison with 0.05 PgC $year^{-2}$)[121], attributed to afforestation-induced greening in the temperate Northern Hemisphere[13,121]. These hotspots of afforestation and forest regrowth are in accordance with the greening pattern observed since 2000 by MODIS (FIG. 2c). Recent DGVM studies[122,123] have further confirmed that the carbon sink during the 2000s was partly driven by afforestation and forest regrowth in East Asia and Europe[124]. The extensive greening over croplands, however, has probably contributed less to the carbon sink, because only a minor portion of assimilated carbon by crops remain sequestered due to crop harvest.

The impact of greening on the carbon cycle is also partly responsible for the increasing seasonality of atmospheric CO_2 in the northern high latitudes[125]. The amplitude of the Northern Hemisphere CO_2 seasonal cycle has increased by as much as 50% for latitudes north of 45°N[126,127] since the 1960s, indicating enhanced vegetation productivity in northern ecosystems during the carbon-uptake period[128]. The spring zero-crossing date — the time when the detrended seasonal CO_2 variations down-cross the zero line in spring — is a phenological indicator of the timing of early season net carbon uptake[125,129]. From 1987 to 2009, the spring zero-crossing date has advanced at high-latitude stations[130] (from −0.5 days $decade^{-1}$ to −1.8 days $decade^{-1}$) (FIG. 3d), a trend that is consistent with the advancing SOS (FIG. 3b). At the end of the net carbon-uptake period, the autumn zero-crossing dates of detrended seasonal CO_2 variations — the time when the detrended seasonal CO_2 variations up-cross the zero line in autumn — have also advanced over eight of the ten Northern Hemisphere stations studied[131]. The observed autumn zero-crossing date advancement (FIG. 3d) is in contrast to the delayed EOS (FIG. 3a) in autumn. This divergence in the autumnal CO_2 and greenness trends suggests that, unlike in spring, autumn vegetation greening does not lead to an increased carbon sink because respiration is increasing more quickly than photosynthesis in autumn[131]. Visual observations (for example, from the Pan European Phenology Project PEP725) and cameras (for example, PhenoCam datasets) are providing an increasing amount of ground-based phenological evidence of this process. In the future, these data can be paired with eddy covariance flux data, to further our mechanistic understanding of the climate-change-induced seasonal change in greenness and carbon balance.

Biogeophysical impacts of greening

Greening has discernable impacts on the hydrologic cycle and climate through modifying surface biogeophysical properties (for example, albedo, evapotranspiration (ET) and surface roughness) on local to regional and global scales[19,132] (FIG. 7). Vegetation's biogeophysical feedbacks to climate are, thus, critical to understanding the potential of ecosystem management, such as afforestation, for climate change mitigation[3,132,133]. In this section, we present the feedbacks of vegetation

Evapotranspiration
The flux of water emitted from the Earth's surface to the atmosphere. It is the sum of evaporation by the soil, wet canopy, open-water surfaces and transpiration by plant stomata.

Transpiration
The loss of water from plants to the atmosphere.

greening on the hydrologic cycle and land-surface air temperature.

The hydrologic cycle. Vegetation greening modulates water cycling. Land water losses to the atmosphere occur through ET, which includes transpiration (60–90% of the total land ET[134–136]) and evaporation. Greening increases water losses through an extended area of leaves performing transpiration[137]. A larger foliage area reduces the bare ground surface from which soil evaporation occurs, but increases the re-evaporation of rainfall intercepted by leaves[138], so that greening can cause the net evaporation to either increase or decrease. Various remote-sensing-based ET estimates consistently point to a significant increase in global terrestrial ET over the past four decades, suggesting an intensified water exchange between the land and the atmosphere concurrent with the greening trend[139]. More than half of the global ET increase since the 1980s has been attributed to vegetation greening[138,139] (FIG. 7).

By controlling the changes in ET, vegetation greening also alters the water distribution between regions and water pools (for example, water in soil, rivers and the atmosphere). Assuming that precipitation does not change in response to vegetation greening, a greening-induced ET increase will reduce soil moisture and runoff, which can intensify droughts at the catchment scale[140,141]. In China's Loess Plateau for instance, where intensive afforestation is associated with a pronounced local greening, the river discharge has indeed decreased by a rate of 0.25 km^3 $year^{-2}$ over the past six decades[142]. However, when using ESMs that consider both the greening-induced ET increase and consequent changes in precipitation, simulations forced only with satellite-observed LAI trends do not generate dramatic changes in soil moisture or runoff at continental or global scales[143,144]. This is because greening-induced ET enhancement increases atmospheric water vapour content, which, in turn, promotes downwind precipitation[145,146]. The enhanced precipitation over transpiring regions is particularly evident in moist forests[147] like the Amazon or Congo, which are 'closed' atmospheric systems where 80% of the rainfall originates from upwind ET[145]. Such an efficient atmospheric water recycling mitigates water loss from the soil, sustains inland vegetation and maintains mesic and humid ecosystems.

In addition to intensifying water cycling at the annual scale, vegetation greening also induces seasonal hydrologic changes. There is emerging evidence that spring-greening-enhanced ET leads to a reduction in soil moisture content, which carries over into the following summer and likely suppresses vegetation growth and increases the risk of heatwaves[148,149]. The greening-induced water loss through ET is recycled as land precipitation in subsequent months, benefitting some remote regions through modulating large-scale atmospheric circulation patterns, despite often being insufficient to compensate for evaporative water loss locally[149]. Proposed climate-mitigation strategies, such as afforestation, therefore need to fully consider coupling between vegetation and other components of the Earth system.

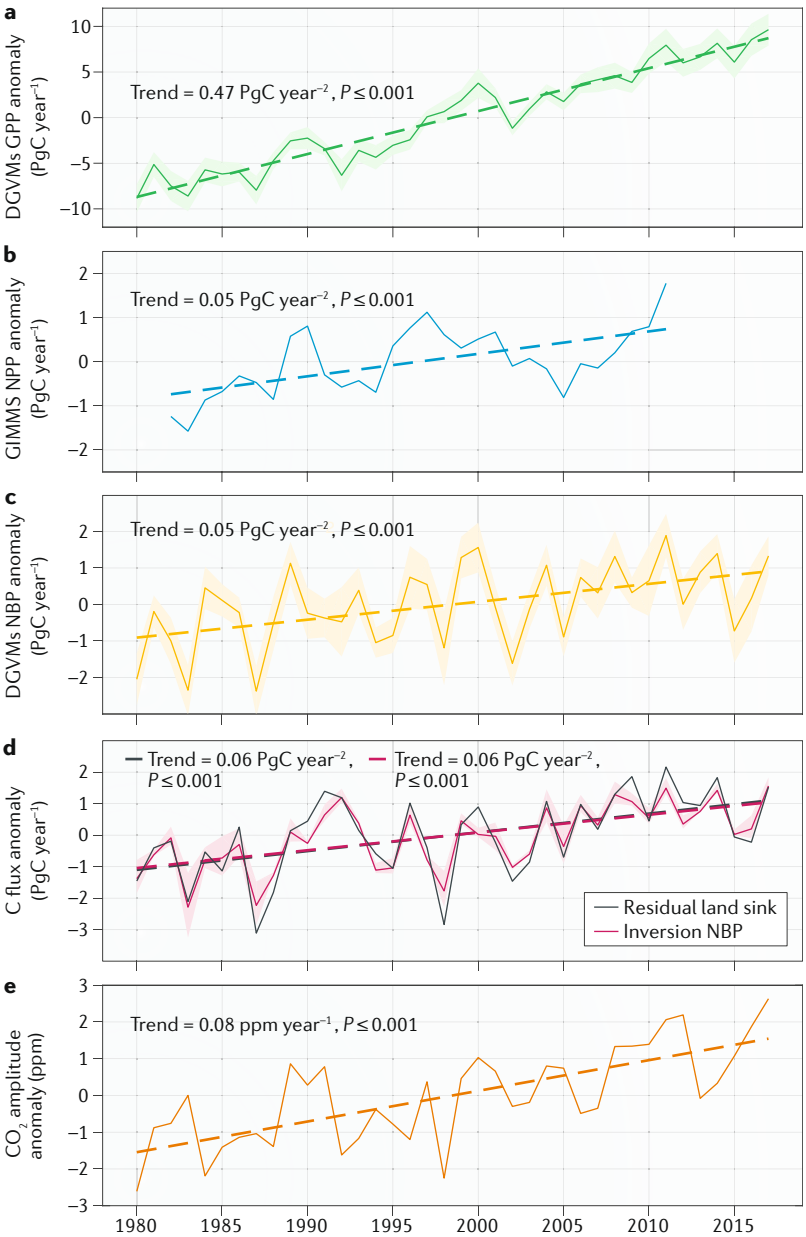

Fig. 6 | **Changes in global carbon fluxes and seasonal CO_2 amplitude.** Graphs depict changes in Barrow, AK, USA, since 1980. **a** | Global gross primary production (GPP). **b** | Net primary production. **c** | Net biome production (NBP). **d** | Residual land sink. **e** | Seasonal CO_2 amplitude. The GPP is from the ensemble mean of 16 dynamic global vegetation models (DGVMs)[111]. The NPP is from greenness-based modelling by Smith et al.[198]. The NBP is from the ensemble mean of 16 DGVMs and two atmospheric inversions[111]. Residual land sink is the mass balance residual of anthropogenic CO_2 emissions, the atmospheric CO_2 growth rate and the ocean CO_2 budget[111]. The shaded areas indicate the standard deviation of the GPP, NPP or NBP across models. The dashed lines indicate linear trends.

Land-surface air temperatures. Greening impacts the exchange of energy between the land and the atmosphere, which ultimately leads to modifications in surface air temperature[150]. Greening increases ET, which cools the surface through evaporative cooling[19,150], but greener canopies have a lower albedo than bare ground and absorb more sunlight, which can result in a larger sensible heat flux. This enhanced sensible heat warms the land surface, an effect called albedo warming[151].

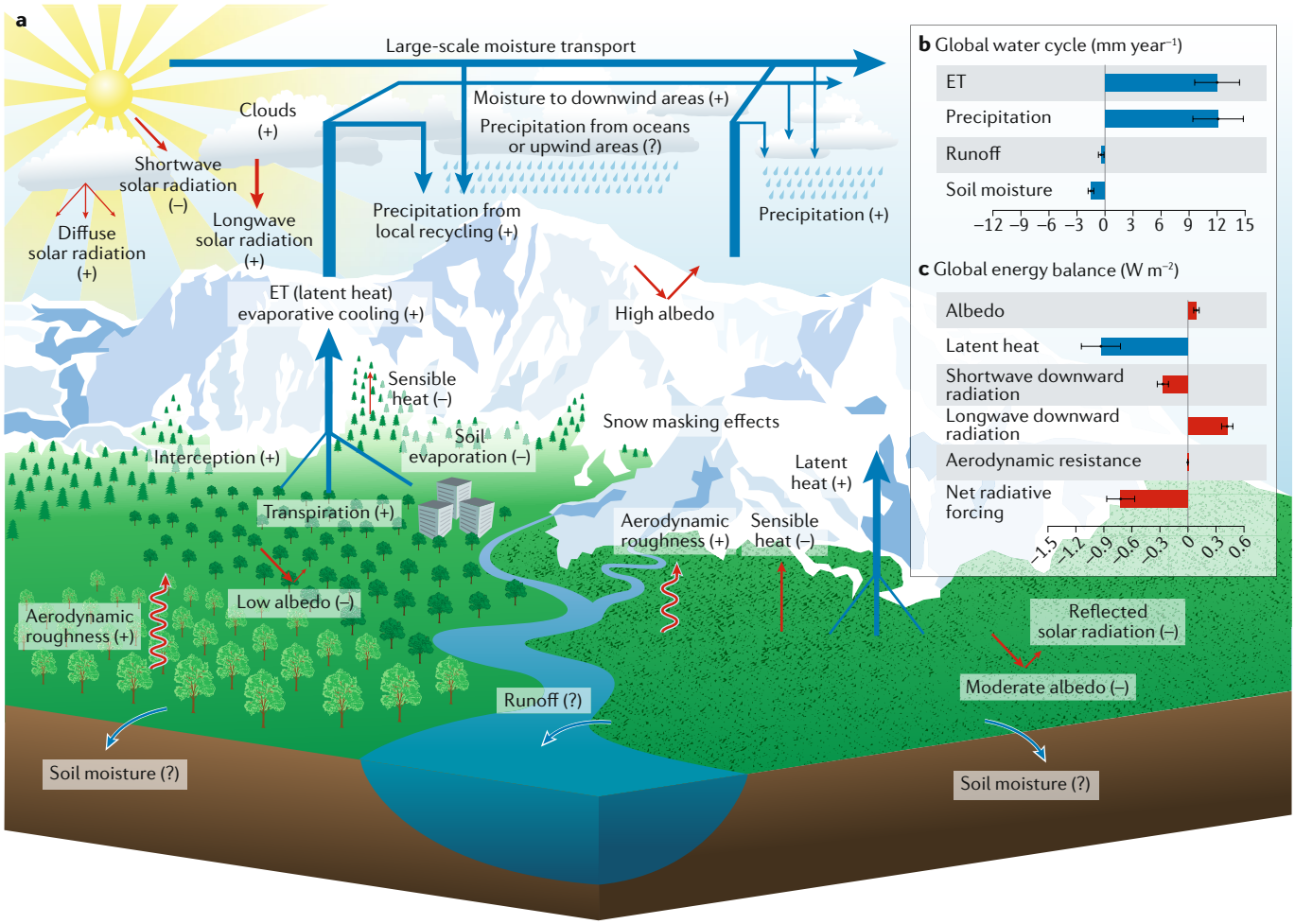

Fig. 7 | **Biogeophysical feedbacks of recent vegetation greening to the climate system. a** | Schematic diagram summarizing land-surface and atmospheric processes through which changes in vegetation greenness feed back into the climate system. For each process or flux, the corresponding symbols '–', '+' and '?' in brackets represent an increasing, decreasing and unknown trend, respectively, in response to vegetation greening, and the colour of arrows represents impacts on water (blue) or energy balance (red, except the latent heat in blue). **b** | Summary of greening-induced changes in major global water cycle fluxes in mm year^{-1} from 1982 to 2011. Data courtesy of Zeng et al.[19]. **c** | Summary of greening-induced changes in global surface energy balance in W m^{-2} from 1982 to 2011. Data courtesy of Zeng et al.[144]. The error bars show the standard error of the estimates. The bar colours are the same as the corresponding fluxes shown in part **a**. ET, evapotranspiration.

The net effect of greening on surface air temperature in many cases can be viewed as the balance between evaporative cooling and albedo warming[152,153], which was estimated globally to be −0.9 W m^{-2} from evaporative cooling and +0.1 W m^{-2} from albedo warming[19] (FIG. 7c).

Greening can also trigger a series of changes through atmospheric circulation that indirectly affect the surface temperature[154]. For example, the additionally transpired water enhances atmospheric water vapour content, which results in more longwave solar radiation entrapment and re-emission in the atmosphere, but reduces the amount of shortwave solar radiation reaching the Earth's surface through increased cloud formation[19,155,156] (FIG. 7). When all the aforementioned impacts of vegetation greening on near-surface air temperature were simulated in coupled ESMs driven by the satellite-based greening since the 1980s, the results suggested a net cooling trend by 12% ± 3% of the concurrent observed warming rate[19].

In warm regions such as the tropics and subtropics, evaporative cooling effects are generally larger than albedo warming effects, leading to a net cooling effect when vegetation greenness increases[19,157,158]. However, the net effect of greening on surface air temperature over the Northern Hemisphere extratropical regions is still subject to debate. Studies based on idealized afforestation and/or deforestation experiments[1,159] or comparisons of the energy budget differences between paired forest and short vegetation sites[132,153] suggested that the albedo warming effect plays a dominant role. These studies, though, assumed complete land cover changes, whereas greening can be gradual. By integrating satellite observations with ESMs, several studies provided an alternative approach that more realistically simulated the effects of vegetation greenness changes and isolated the signal of climate response to greening. These studies found that greening slowed down warming through

evaporative cooling in Arctic and boreal regions[19], the Tibetan Plateau[160] and temperate regions like East Asia[161]. Nonetheless, current state-of-the-art modelling efforts are still inconclusive, as some processes are not yet well represented in ESMs, such as snow masking by greener canopies during cold seasons[162–164] and the partitioning of transpiration and evaporation that is sensitive to vegetation greenness change[136]. Since most ESMs underestimate the ratio of transpiration to ET[136], evaporative cooling by greening could have been underestimated[19,133].

Conclusions

Widespread vegetation greening since the 1980s is one of the most notable characteristics of biosphere change in the Anthropocene. Greening has significantly enhanced the land carbon sink, intensified the hydrologic cycle and cooled the land surface at the global scale. A mechanistic understanding of the underlying drivers shows how anthropogenic forcing has fundamentally altered today's Earth system through a set of feedback loops. Improved knowledge of greenness changes, together with recent progress in observing technology and modelling capacity, has resulted in major advances in understanding global vegetation dynamics. Nonetheless, we still face many challenges ahead.

One key challenge is to continue developing the capacity of remote sensing to measure vegetation structure and functions. Although the vegetation greenness indices described in this Review have proved highly reliable, contemporary satellite greenness products still suffer from limitations, such as inadequate sensitivity to detect changes in dense vegetation, aliasing between snow cover decrease and leaf area increase in cold ecosystems (such as boreal forests), atmospheric contamination, orbital drift and sensor replacements. Compared with the AVHRR, the new moderate-resolution spectral bands and spatial resolutions of 250 m to 1 km of the MODIS sensors on board the Terra (operating since 1999) and Aqua (operating since 2002) satellites have provided global datasets that largely improved the long-term monitoring of vegetation greenness[13]. The current scientific community needs to include Earth observations with higher temporal, richer spectral and finer spatial resolutions to capture various ecosystem functions and processes responding to different parts of the electromagnetic spectrum[165]. We expect the development of next-generation satellite missions and vegetation indices to better fulfil these needs. For example, ongoing efforts on developing hyperspectral remote sensing such as the EnMAP, FLEX and HyspIRI missions will improve the richness and specificity of spectral information on vegetation structure and functioning.

Another equally important challenge is to validate satellite-based greenness changes with ground observations. Currently, the lack of systematic long-term ground observations covering a large spatial gradient from the high Arctic to the tropics has led to few available ground truths[166] to confirm greenness changes detected through satellite products. Therefore, expanding existing observational networks (such as PhenoCam and FLUXNET) is a high priority. For example, the mismatch between the spatial distribution of vegetation productivity and the density of FLUXNET sites[167] highlights the need to expand the current network from the mid-latitudes to the tropics, where the most photosynthesis takes place. Also, growing crowd-sourced observations by citizen scientists, such as the CrowdCurio phenology observations over the eastern USA[168], can provide valuable data that complement the more expensive professional ground observation networks. These increasing types and amounts of data, together with the rapid development of deep learning[169] and process modelling[11], offer promising tools for improving our understanding of vegetation greening[169].

Considerable uncertainties remain in ESM projections on if and where vegetation greening will occur. Recent studies have identified several processes causing vegetation browning in some regions, including forest diebacks[170], insect[35] and disease outbreaks[171], thermokarst development[172], human mismanagement[36,173], destructive logging[174] and industrial development[175]. These emerging threats could lead to unexpected changes in vegetation greenness relative to our current projections (such as the projections shown in FIGS 2e–h,5), since these processes are under-represented in ESMs. Thus, integrating continued space and ground monitoring and advancing ESM developments is a critical cross-sectoral research priority.

Published online: 09 December 2019

1. Bonan, G. B., Pollard, D. & Thompson, S. L. Effects of boreal forest vegetation on global climate. *Nature* **359**, 716–718 (1992).
2. Haberl, H. et al. Quantifying and mapping the human appropriation of net primary production in earth's terrestrial ecosystems. *Proc. Natl Acad. Sci. USA* **104**, 12942–12947 (2007).
3. Griscom, B. W. et al. Natural climate solutions. *Proc. Natl Acad. Sci. USA* **114**, 11645–11650 (2017).
4. Bastin, J.-F. et al. The global tree restoration potential. *Science* **365**, 76–79 (2019).
5. Tucker, C. J., Fung, I. Y., Keeling, C. D. & Gammon, R. H. Relationship between atmospheric CO_2 variations and a satellite-derived vegetation index. *Nature* **319**, 195–199 (1986).
6. Fung, I. Y., Tucker, C. J. & Prentice, K. C. Application of advanced very high resolution radiometer vegetation index to study atmosphere-biosphere exchange of CO_2. *J. Geophys. Res. Atmos.* **92**, 2999–3015 (1987).
7. Myneni, R. B., Keeling, C. D., Tucker, C. J., Asrar, G. & Nemani, R. R. Increased plant growth in the northern high latitudes from 1981 to 1991. *Nature* **386**, 698–702 (1997).
The first study to reveal large-scale vegetation greening over the Northern Hemisphere.
8. Zhou, L. et al. Variations in northern vegetation activity inferred from satellite data of vegetation index during 1981 to 1999. *J. Geophys. Res. Atmos.* **106**, 20069–20083 (2001).
9. Goetz, S. J., Bunn, A. G., Fiske, G. J. & Houghton, R. A. Satellite-observed photosynthetic trends across boreal North America associated with climate and fire disturbance. *Proc. Natl Acad. Sci. USA* **102**, 13521–13525 (2005).
10. Xu, L. et al. Temperature and vegetation seasonality diminishment over northern lands. *Nat. Clim. Change* **3**, 581–586 (2013).
11. Zhu, Z. et al. Greening of the Earth and its drivers. *Nat. Clim. Change* **6**, 791–795 (2016).
A detailed attribution study of global leaf area index change during the past three decades with ensemble dynamic global vegetation models.
12. Ju, J. & Masek, J. G. The vegetation greenness trend in Canada and US Alaska from 1984–2012 Landsat data. *Remote. Sens. Environ.* **176**, 1–16 (2016).
13. Chen, C. et al. China and India lead in greening of the world through land-use management. *Nat. Sustain.* **2**, 122–129 (2019).
Demonstrates the pattern of global greening since 2000 with the latest MODIS C6 collection data.
14. Lucht, W. et al. Climatic control of the high-latitude vegetation greening trend and Pinatubo effect. *Science.* **296**, 1687–1689 (2002).
15. Arneth, A. et al. IPCC special report on climate change and land. *Intergovernmental Panel on Climate Change (IPCC)* https://www.ipcc.ch/report/srccl/ (2019) (accessed October 2019).
16. Abram, N. et al. IPCC special report on the ocean and cryosphere in a changing climate. *Intergovernmental Panel on Climate Change (IPCC)* https://www.ipcc.ch/srocc/home/ (accessed October 2019).
17. Eyring, V. et al. Overview of the Coupled Model Intercomparison Project Phase 6 (CMIP6) experimental

design and organization. *Geosci. Model. Dev.* **9**, 1937–1958 (2016).
18. Swann, A. L. S., Fung, I. Y. & Chiang, J. C. H. Mid-latitude afforestation shifts general circulation and tropical precipitation. *Proc. Natl Acad. Sci. USA* **109**, 712–716 (2012).
19. Zeng, Z. et al. Climate mitigation from vegetation biophysical feedbacks during the past three decades. *Nat. Clim. Change* **7**, 432–436 (2017).
A quantification of the climatic impacts of vegetation greening through modulating land-atmosphere energy and water exchanges, with an Earth system model forced by satellite-observed LAI change during the past three decades.
20. de Jong, R., Verbesselt, J., Schaepman, M. E. & De Bruin, S. Trend changes in global greening and browning: contribution of short-term trends to longer-term change. *Glob. Change Biol.* **18**, 642–655 (2012).
21. Tian, F. et al. Evaluating temporal consistency of long-term global NDVI datasets for trend analysis. *Remote. Sens. Environ.* **163**, 326–340 (2015).
22. Zhang, Y., Song, C., Band, L. E., Sun, G. & Li, J. Reanalysis of global terrestrial vegetation trends from MODIS products: Browning or greening? *Remote. Sens. Environ.* **191**, 145–155 (2017).
23. Liu, Y., Liu, R. & Chen, J. M. Retrospective retrieval of long-term consistent global leaf area index (1981–2011) from combined AVHRR and MODIS data. *J. Geophys. Res. Biogeosciences* **117**, G04003 (2012).
24. Lyapustin, A. et al. Scientific impact of MODIS C5 calibration degradation and C6+ improvements. *Atmos. Meas. Tech.* **7**, 4353–4365 (2014).
25. Park, T. et al. Changes in growing season duration and productivity of northern vegetation inferred from long-term remote sensing data. *Environ. Res. Lett.* **11**, 084001 (2016).
26. Beck, P. S. A. & Goetz, S. J. Satellite observations of high northern latitude vegetation productivity changes between 1982 and 2008: ecological variability and regional differences. *Environ. Res. Lett.* **6**, 045501 (2011).
27. Sturm, M., Racine, C. & Tape, K. Climate change: increasing shrub abundance in the Arctic. *Nature* **411**, 546–547 (2001).
28. Frost, G. V. & Epstein, H. E. Tall shrub and tree expansion in Siberian tundra ecotones since the 1960s. *Glob. Change Biol.* **20**, 1264–1277 (2014).
29. Myers-Smith, I. H. et al. Climate sensitivity of shrub growth across the tundra biome. *Nat. Clim. Change* **5**, 887–891 (2015).
30. Myers-Smith, I. H. et al. Shrub expansion in tundra ecosystems: dynamics, impacts and research priorities. *Environ. Res. Lett.* **6**, 045509 (2011).
31. Mahowald, N. et al. Projections of leaf area index in earth system models. *Earth Syst. Dyn.* **7**, 211–229 (2016).
32. Bhatt, U. et al. Recent declines in warming and vegetation greening trends over pan-Arctic tundra. *Remote. Sens.* **5**, 4229–4254 (2013).
33. Verbyla, D. The greening and browning of Alaska based on 1982–2003 satellite data. *Glob. Ecol. Biogeogr.* **17**, 547–555 (2008).
34. Senf, C., Pflugmacher, D., Wulder, M. A. & Hostert, P. Characterizing spectral–temporal patterns of defoliator and bark beetle disturbances using Landsat time series. *Remote. Sens. Environ.* **170**, 166–177 (2015).
35. Bjerke, J. W. et al. Understanding the drivers of extensive plant damage in boreal and Arctic ecosystems: Insights from field surveys in the aftermath of damage. *Sci. Total. Environ.* **599**, 1965–1976 (2017).
36. White, J. C., Wulder, M. A., Hermosilla, T., Coops, N. C. & Hobart, G. W. A nationwide annual characterization of 25 years of forest disturbance and recovery for Canada using Landsat time series. *Remote. Sens. Environ.* **194**, 303–321 (2017).
37. Sulla-Menashe, D., Woodcock, C. E. & Friedl, M. A. Canadian boreal forest greening and browning trends: an analysis of biogeographic patterns and the relative roles of disturbance versus climate drivers. *Environ. Res. Lett.* **13**, 014007 (2018).
38. Bi, J., Xu, L., Samanta, A., Zhu, Z. & Myneni, R. Divergent Arctic-boreal vegetation changes between North America and Eurasia over the past 30 years. *Remote. Sens.* **5**, 2093–2112 (2013).
39. Feng, X. et al. Revegetation in China's Loess Plateau is approaching sustainable water resource limits. *Nat. Clim. Change.* **6**, 1019–1022 (2016).
40. Zhou, L. et al. Widespread decline of Congo rainforest greenness in the past decade. *Nature* **509**, 86–90 (2014).
41. Goswami, S., Gamon, J., Vargas, S. & Tweedie, C. Relationships of NDVI, biomass, and leaf area index (LAI) for six key plant species in Barrow, Alaska. *PeerJ PrePrints* **3**, e913v1 (2015).
42. Samanta, A. et al. Amazon forests did not green-up during the 2005 drought. *Geophys. Res. Lett.* **37**, L05401 (2010).
43. Saleska, S. R., Didan, K., Huete, A. R. & Da Rocha, H. R. Amazon forests green-up during 2005 drought. *Science* **318**, 612 (2007).
44. Asner, G. P. & Alencar, A. Drought impacts on the Amazon forest: the remote sensing perspective. *New Phytol.* **187**, 569–578 (2010).
45. Fensholt, R. et al. Greenness in semi-arid areas across the globe 1981–2007—an Earth Observing Satellite based analysis of trends and drivers. *Remote. Sens. Environ.* **121**, 144–158 (2012).
46. Ahlström, A. et al. The dominant role of semi-arid ecosystems in the trend and variability of the land CO_2 sink. *Science* **348**, 895–899 (2015).
47. Buitenwerf, R., Rose, L. & Higgins, S. I. Three decades of multi-dimensional change in global leaf phenology. *Nat. Clim. Change* **5**, 364–368 (2015).
48. Piao, S. et al. Plant phenology and global climate change: current progresses and challenges. *Glob. Change Biol.* **25**, 1922–1940 (2019).
49. White, M. A. et al. Intercomparison, interpretation, and assessment of spring phenology in North America estimated from remote sensing for 1982–2006. *Glob. Change Biol.* **15**, 2335–2359 (2009).
50. Schwartz, M. D. & Hanes, J. M. Intercomparing multiple measures of the onset of spring in eastern North America. *Int. J. Climatol.* **30**, 1614–1626 (2010).
51. Richardson, A. D., Hufkens, K., Milliman, T. & Frolking, S. Intercomparison of phenological transition dates derived from the PhenoCam Dataset V1.0 and MODIS satellite remote sensing. *Sci. Rep.* **8**, 5679 (2018).
52. Jeong, S.-J., Ho, C.-H., Gim, H.-J. & Brown, M. E. Phenology shifts at start vs. end of growing season in temperate vegetation over the Northern Hemisphere for the period 1982–2008. *Glob. Change Biol.* **17**, 2385–2399 (2011).
53. Keenan et al. Net carbon uptake has increased through warming-induced changes in temperate forest phenology. *Nat. Clim. Change* **4**, 598–604 (2014).
54. Garonna, I., de Jong, R. & Schaepman, M. E. Variability and evolution of global land surface phenology over the past three decades (1982–2012). *Glob. Change Biol.* **22**, 1456–1468 (2016).
55. Menzel, A. et al. European phenological response to climate change matches the warming pattern. *Glob. Change Biol.* **12**, 1969–1976 (2006).
56. Cleland, E. E., Chuine, I., Menzel, A., Mooney, H. A. & Schwartz, M. D. Shifting plant phenology in response to global change. *Trends Ecol. Evol.* **22**, 357–365 (2007).
57. Gill, A. L. et al. Changes in autumn senescence in northern hemisphere deciduous trees: a meta-analysis of autumn phenology studies. *Ann. Bot.* **116**, 875–888 (2015).
58. Barichivich, J. et al. Large-scale variations in the vegetation growing season and annual cycle of atmospheric CO_2 at high northern latitudes from 1950 to 2011. *Glob. Change Biol.* **19**, 3167–3183 (2013).
59. Piao, S., Friedlingstein, P., Ciais, P., Viovy, N. & Demarty, J. Growing season extension and its impact on terrestrial carbon cycle in the Northern Hemisphere over the past 2 decades. *Glob. Biogeochem. Cycles* **21**, GB3018 (2007).
60. Julien, Y. & Sobrino, J. A. Global land surface phenology trends from GIMMS database. *Int. J. Remote. Sens.* **30**, 3495–3513 (2009).
61. Park, T. et al. Changes in timing of seasonal peak photosynthetic activity in northern ecosystems. *Glob. Change Biol.* **25**, 2382–2395 (2019).
62. Gonsamo, A., Chen, J. M. & Ooi, Y. W. Peak season plant activity shift towards spring is reflected by increasing carbon uptake by extratropical ecosystems. *Glob. Change Biol.* **24**, 2117–2128 (2018).
63. Bhatt, U. S. et al. Changing seasonality of panarctic tundra vegetation in relationship to climatic variables. *Environ. Res. Lett.* **12**, 055003 (2017).
64. Epstein, H. et al. Tundra greenness. In Arctic Report Card 2018. National Oceanic and Atmospheric Administration (NOAA), 46–52 (2018).
65. Huang, M. et al. Velocity of change in vegetation productivity over northern high latitudes. *Nat. Ecol. Evol.* **1**, 1649–1654 (2017).
66. Farquhar, G. D. & Sharkey, T. D. Stomatal conductance and photosynthesis. *Annu. Rev. Plant. Physiol.* **33**, 317–345 (1982).
67. Keenan, T. F. et al. Increase in forest water-use efficiency as atmospheric carbon dioxide concentrations rise. *Nature* **499**, 324–327 (2013).
68. Donohue, R. J., Roderick, M. L., McVicar, T. R. & Farquhar, G. D. Impact of CO_2 fertilization on maximum foliage cover across the globe's warm, arid environments. *Geophys. Res. Lett.* **40**, 3031–3035 (2013).
69. Ukkola, A. M., Prentice, I. C., Keenan, T. F., van Dijk, A. I. J. M., Viney, N. R., Myneni, R. B. & Bi, J. Reduced streamflow in water-stressed climates consistent with CO_2 effects on vegetation. *Nat. Clim. Change* **6**, 75–78 (2015).
70. Sitch, S. et al. Recent trends and drivers of regional sources and sinks of carbon dioxide. *Biogeosciences* **12**, 653–679 (2015).
71. Ahlbeck, J. R. Comment on "Variations in northern vegetation activity inferred from satellite data of vegetation index during 1981–1999" by L. Zhou et al. *J. Geophys. Res. Atmos.* **107**, ACH–9 (2002).
72. Los, S. O. Analysis of trends in fused AVHRR and MODIS NDVI data for 1982–2006: Indication for a CO_2 fertilization effect in global vegetation. *Glob. Biogeochem. Cycles* **27**, 318–330 (2013).
73. Norby, R. J., Warren, J. M., Iversen, C. M., Medlyn, B. E. & McMurtrie, R. E. CO_2 enhancement of forest productivity constrained by limited nitrogen availability. *Proc. Natl Acad. Sci.USA* **107**, 19368–19373 (2010).
74. Dubey, S. K., Tripathi, S. K. & Pranuthi, G. Effect of elevated CO_2 on wheat crop: Mechanism and impact. *Crit. Rev. Environ. Sci. Technol.* **45**, 2283–2304 (2015).
75. Ainsworth, E. A. & Long, S. P. What have we learned from 15 years of free-air CO_2 enrichment (FACE)? A meta-analytic review of the responses of photosynthesis, canopy properties and plant production to rising CO_2. *New Phytol.* **165**, 351–372 (2005).
76. Norby, R. J. & Zak, D. R. Ecological lessons from free-air CO_2 enrichment (FACE) experiments. *Annu. Rev. Ecol. Evol. Syst.* **42**, 181–203 (2011).
77. Hickler, T. et al. CO_2 fertilization in temperate FACE experiments not representative of boreal and tropical forests. *Glob. Change Biol.* **14**, 1531–1542 (2008).
78. Schimel, D., Stephens, B. B. & Fisher, J. B. Effect of increasing CO_2 on the terrestrial carbon cycle. *Proc. Natl Acad. Sci. USA* **112**, 436–441 (2015).
79. Obermeier, W. A. et al. Reduced CO_2 fertilization effect in temperate C3 grasslands under more extreme weather conditions. *Nat. Clim. Change* **7**, 137–141 (2017).
80. Gray, S. B. et al. Intensifying drought eliminates the expected benefits of elevated carbon dioxide for soybean. *Nat. Plants* **2**, 16132 (2016).
81. Reich, P. B. & Hobbie, S. E. Decade-long soil nitrogen constraint on the CO_2 fertilization of plant biomass. *Nat. Clim. Change* **3**, 278–282 (2013).
82. Reich, P. B., Hobbie, S. E. & Lee, T. D. Plant growth enhancement by elevated CO_2 eliminated by joint water and nitrogen limitation. *Nat. Geosci.* **7**, 920–924 (2014).
83. Terrer, C. et al. Nitrogen and phosphorus constrain the CO_2 fertilization of global plant biomass. *Nat. Clim. Change* **9**, 684–689 (2019).
84. Corlett, R. T. Impacts of warming on tropical lowland rainforests. *Trends Ecol. Evol.* **26**, 606–613 (2011).
85. Huang, M. et al. Air temperature optima of vegetation productivity across global biomes. *Nat. Ecol. Evol.* **3**, 772–779 (2019).
86. Keenan, T. F. & Riley, W. J. Greening of the land surface in the world's cold regions consistent with recent warming. *Nat. Clim. Change* **8**, 825–828 (2018).
87. Braswell, B. H., Schimel, D. S., Linder, E. & Moore, B. III The response of global terrestrial ecosystems to interannual temperature variability. *Science* **278**, 870–873 (1997).
88. Linderholm, H. W. Growing season changes in the last century. *Agric. For. Meteorol.* **137**, 1–14 (2006).
89. Richardson, A. D. et al. Influence of spring and autumn phenological transitions on forest ecosystem productivity. *Philos. Trans. R. Soc. Lond.* **365**, 3227–3246 (2010).
90. Piao, S. et al. Evidence for a weakening relationship between interannual temperature variability and northern vegetation activity. *Nat. Commun.* **5**, 5018 (2014).
Discusses the weakening temperature impacts on northern vegetation greenness since the 1980s.

91. Vickers, H. et al. Changes in greening in the high Arctic: insights from a 30 year AVHRR max NDVI dataset for Svalbard. *Environ. Res. Lett.* **11**, 105004 (2016).
92. Nemani, R. R. et al. Climate-driven increases in global terrestrial net primary production from 1982 to 1999. *Science* **300**, 1560–1563 (2003).
93. Eklundh, L. & Olsson, L. Vegetation index trends for the African Sahel 1982–1999. *Geophys. Res. Lett.* **30**, 1430 (2003).
94. Anyamba, A. & Tucker, C. J. Analysis of Sahelian vegetation dynamics using NOAA-AVHRR NDVI data from 1981–2003. *J. Arid. Environ.* **63**, 596–614 (2005).
95. Donohue, R. J., McVicar, T. R. & Roderick, M. L. Climate-related trends in Australian vegetation cover as inferred from satellite observations, 1981–2006. *Glob. Change Biol.* **15**, 1025–1039 (2009).
96. Herrmann, S. M., Anyamba, A. & Tucker, C. J. Recent trends in vegetation dynamics in the African Sahel and their relationship to climate. *Glob. Environ. Change* **15**, 394–404 (2005).
97. Hickler, T. et al. Precipitation controls Sahel greening trend. *Geophys. Res. Lett.* **32**, L21415 (2005).
98. Huber, S., Fensholt, R. & Rasmussen, K. Water availability as the driver of vegetation dynamics in the African Sahel from 1982 to 2007. *Glob. Planet. Change* **76**, 186–195 (2011).
99. Dardel, C. et al. Re-greening Sahel: 30 years of remote sensing data and field observations (Mali, Niger). *Remote. Sens. Environ.* **140**, 350–364 (2014).
100. Brandt, M. et al. Changes in rainfall distribution promote woody foliage production in the Sahel. *Commun. Biol.* **2**, 133 (2019).
101. Brandt, M. et al. Human population growth offsets climate-driven increase in woody vegetation in sub-Saharan Africa. *Nat. Ecol. Evol.* **1**, 0081 (2017).
102. Curtis, P. G., Slay, C. M., Harris, N. L., Tyukavina, A. & Hansen, M. C. Classifying drivers of global forest loss. *Science* **361**, 1108–1111 (2018).
103. Eighth National Forest Resource Inventory Report (2009–2013) (State Forestry Administration of the People's Republic of China, 2014).
104. Luyssaert, S. et al. Land management and land-cover change have impacts of similar magnitude on surface temperature. *Nat. Clim. Change* **4**, 389–393 (2014).
105. Song, X.-P. et al. Global land change from 1982 to 2016. *Nature* **560**, 639–643 (2018).
106. Poulter, B. et al. The global forest age dataset and its uncertainties (GFADv1.1). *NASA National Aeronautics and Space Administration, PANGAEA* https://doi.org/10.1594/PANGAEA.897392 (2019).
107. Reich, P. B. et al. Nitrogen limitation constrains sustainability of ecosystem response to CO_2. *Nature* **440**, 922–925 (2006).
108. Penuelas, J. et al. Human-induced nitrogen–phosphorus imbalances alter natural and managed ecosystems across the globe. *Nat. Commun.* **4**, 2934 (2013).
109. Greaver, T. L. et al. Key ecological responses to nitrogen are altered by climate change. *Nat. Clim. Change* **6**, 836–843 (2016).
110. Zaehle, S. et al. Evaluation of 11 terrestrial carbon–nitrogen cycle models against observations from two temperate Free-Air CO_2 Enrichment studies. *New Phytol.* **202**, 803–822 (2014).
111. Le Quéré, C. et al. Global carbon budget 2018. *Earth Syst. Sci. Data* **10**, 2141–2194 (2018).
112. Chen, J. M. et al. Vegetation structural change since 1981 significantly enhanced the terrestrial carbon sink. *Nat. Commun.* **10**, 4259 (2019).
113. van Dijk, A. I. J. M., Dolman, A. J. & Schulze, E.-D. Radiation, temperature, and leaf area explain ecosystem carbon fluxes in boreal and temperate European forests. *Glob. Biogeochem. Cycles* **19**, GB2029 (2005).
114. Zhang, Y., Joiner, J., Alemohammad, S. H., Zhou, S. & Gentine, P. A global spatially contiguous solar-induced fluorescence (CSIF) dataset using neural networks. *Biogeosciences* **15**, 5779–5800 (2018).
115. Cheng, L. et al. Recent increases in terrestrial carbon uptake at little cost to the water cycle. *Nat. Commun.* **8**, 110 (2017).
116. Winkler, A. J., Myneni, R. B., Alexandrov, G. A. & Brovkin, V. Earth system models underestimate carbon fixation by plants in the high latitudes. *Nat. Commun.* **10**, 885 (2019).
117. Shevliakova, E. et al. Historical warming reduced due to enhanced land carbon uptake. *Proc. Natl Acad. Sci. USA* **110**, 16730–16735 (2013).
118. Pan, Y. et al. A large and persistent carbon sink in the world's forests. *Science* **333**, 988–993 (2011).
119. Liu, Y. Y. et al. Recent reversal in loss of global terrestrial biomass. *Nat. Clim. Change* **5**, 470–474 (2015).
120. Keenan, T. F. et al. Recent pause in the growth rate of atmospheric CO_2 due to enhanced terrestrial carbon uptake. *Nat. Commun.* **7**, 13428 (2016).
121. Piao, S. et al. Lower land-use emissions responsible for increased net land carbon sink during the slow warming period. *Nat. Geosci.* **11**, 739–743 (2018).
122. Kondo, M. et al. Plant regrowth as a driver of recent enhancement of terrestrial CO_2 uptake. *Geophys. Res. Lett.* **45**, 4820–4830 (2018).
123. Pugh, T. A. M. et al. Role of forest regrowth in global carbon sink dynamics. *Proc. Natl Acad. Sci. USA* **116**, 4382–4387 (2019).
124. Naudts, K. et al. Europe's forest management did not mitigate climate warming. *Science* **351**, 597–600 (2016).
125. Keeling, C. D., Chin, J. F. S. & Whorf, T. P. Increased activity of northern vegetation inferred from atmospheric CO_2 measurements. *Nature* **382**, 146–149 (1996).
126. Graven, H. D. et al. Enhanced seasonal exchange of CO_2 by northern ecosystems since 1960. *Science* **341**, 1085–1089 (2013).
127. Piao, S. et al. On the causes of trends in the seasonal amplitude of atmospheric CO_2. *Glob. Change Biol.* **24**, 608–616 (2018).
128. Forkel, M. et al. Enhanced seasonal CO_2 exchange caused by amplified plant productivity in northern ecosystems. *Science* **351**, 696–699 (2016).
Presents the linkage between increasing photosynthesis of northern vegetation and the enlarging seasonal CO_2 amplitude.
129. Piao, S. et al. Weakening temperature control on the interannual variations of spring carbon uptake across northern lands. *Nat. Clim. Change* **7**, 359–363 (2017).
130. Barichivich, J., Briffa, K. R., Osborn, T. J., Melvin, T. M. & Caesar, J. Thermal growing season and timing of biospheric carbon uptake across the Northern Hemisphere. *Glob. Biogeochem. Cycles* **26**, GB4015 (2012).
131. Piao, S. et al. Net carbon dioxide losses of northern ecosystems in response to autumn warming. *Nature* **451**, 49–52 (2008).
132. Alkama, R. & Cescatti, A. Biophysical climate impacts of recent changes in global forest cover. *Science* **351**, 600–604 (2016).
Presents evidence for feedbacks of forest cover change to land-surface temperature and its regional disparities.
133. Arora, V. K. & Montenegro, A. Small temperature benefits provided by realistic afforestation efforts. *Nat. Geosci.* **4**, 514–518 (2011).
134. Jasechko, S. et al. Terrestrial water fluxes dominated by transpiration. *Nature* **496**, 347–350 (2013).
135. Good, S. P., Noone, D. & Bowen, G. Hydrologic connectivity constrains partitioning of global terrestrial water fluxes. *Science* **349**, 175–177 (2015).
136. Lian, X. et al. Partitioning global land evapotranspiration using CMIP5 models constrained by observations. *Nat. Clim. Change* **8**, 640–646 (2018).
137. Bernacchi, C. J. & VanLoocke, A. Terrestrial ecosystems in a changing environment: a dominant role for water. *Annu. Rev. Plant. Biol.* **66**, 599–622 (2015).
138. Zhang, Y. et al. Multi-decadal trends in global terrestrial evapotranspiration and its components. *Sci. Rep.* **6**, 19124 (2016).
139. Zeng, Z., Peng, L. & Piao, S. Response of terrestrial evapotranspiration to Earth's greening. *Curr. Opin. Environ. Sustain.* **33**, 9–25 (2018).
140. Bosch, J. M. & Hewlett, J. D. A review of catchment experiments to determine the effect of vegetation changes on water yield and evapotranspiration. *J. Hydrol.* **55**, 3–23 (1982).
141. Evaristo, J. & McDonnell, J. J. Global analysis of streamflow response to forest management. *Nature* **570**, 455–461 (2019).
142. Wang, S. et al. Reduced sediment transport in the Yellow River due to anthropogenic changes. *Nat. Geosci.* **9**, 38–41 (2016).
143. Li, Y. et al. Divergent hydrological response to large-scale afforestation and vegetation greening in China. *Sci. Adv.* **4**, eaar4182 (2018).
144. Zeng, Z. et al. Impact of Earth greening on the terrestrial water cycle. *J. Clim.* **31**, 2633–2650 (2018).
145. van der Ent, R. J., Savenije, H. H. G., Schaefli, B. & Steele-Dunne, S. C. Origin and fate of atmospheric moisture over continents. *Water Resour. Res.* **46**, W09525 (2010).
Discusses the importance of land evapotranspiration to sustain downwind precipitation.
146. Teuling, A. J. et al. Observational evidence for cloud cover enhancement over western European forests. *Nat. Commun.* **8**, 14065 (2017).
147. Spracklen, D. V., Arnold, S. R. & Taylor, C. M. Observations of increased tropical rainfall preceded by air passage over forests. *Nature* **489**, 282–285 (2012).
148. Buermann, W. et al. Widespread seasonal compensation effects of spring warming on northern plant productivity. *Nature* **562**, 110–114 (2018).
149. Lian, X. et al. Summer soil drying exacerbated by earlier spring greening of northern vegetation. *Sci. Adv.* (in the press) https://doi.org/10.1126/sciadv.aax0255.
150. Bonan, G. B. Forests, climate, and public policy: A 500-year interdisciplinary odyssey. *Annu. Rev. Ecol. Evol. Syst.* **47**, 97–121 (2016).
151. Davin, E. L. & de Noblet-Ducoudré, N. Climatic impact of global-scale deforestation: Radiative versus nonradiative processes. *J. Clim.* **23**, 97–112 (2010).
152. Bonan, G. B. Forests and climate change: forcings, feedbacks, and the climate benefits of forests. *Science* **320**, 1444–1449 (2008).
153. Lee, X. et al. Observed increase in local cooling effect of deforestation at higher latitudes. *Nature* **479**, 384–387 (2011).
154. Winckler, J., Lejeune, Q., Reick, C. H. & Pongratz, J. Nonlocal effects dominate the global mean surface temperature response to the biogeophysical effects of deforestation. *Geophys. Res. Lett.* **46**, 745–755 (2019).
155. Green, J. K. et al. Regionally strong feedbacks between the atmosphere and terrestrial biosphere. *Nat. Geosci.* **10**, 410–414 (2017).
156. Devaraju, N., de Noblet-Ducoudré, N., Quesada, B. & Bala, G. Quantifying the relative importance of direct and indirect biophysical effects of deforestation on surface temperature and teleconnections. *J. Clim.* **31**, 3811–3829 (2018).
157. Bateni, S. M. & Entekhabi, D. Relative efficiency of land surface energy balance components. *Water Resour. Res.* **48**, 4510 (2012).
158. Forzieri, G., Alkama, R., Miralles, D. G. & Cescatti, A. Satellites reveal contrasting responses of regional climate to the widespread greening of Earth. *Science* **356**, 1180–1184 (2017).
159. Betts, R. A. Offset of the potential carbon sink from boreal forestation by decreases in surface albedo. *Nature* **408**, 187–190 (2000).
160. Shen, M. et al. Evaporative cooling over the Tibetan Plateau induced by vegetation growth. *Proc. Natl Acad. Sci. USA* **112**, 9299–9304 (2015).
161. Jeong, S., Ho, C., Kim, K. & Jeong, J. Reduction of spring warming over East Asia associated with vegetation feedback. *Geophys. Res. Lett.* **36**, L18705 (2009).
162. Essery, R. Large-scale simulations of snow albedo masking by forests. *Geophys. Res. Lett.* **40**, 5521–5525 (2013).
163. Thackeray, C. W., Fletcher, C. G. & Derksen, C. The influence of canopy snow parameterizations on snow albedo feedback in boreal forest regions. *J. Geophys. Res. Atmos.* **119**, 9810–9821 (2014).
164. Wang, L. et al. Investigating the spread in surface albedo for snow-covered forests in CMIP5 models. *J. Geophys. Res. Atmos.* **121**, 1104–1119 (2016).
165. National Academies of Sciences, Engineering, and Medicine. Thriving on our changing planet: A decadal strategy for Earth observation from space (National Academies Press, 2018) https://doi.org/10.17226/24938.
166. Metcalfe, D. B. et al. Patchy field sampling biases understanding of climate change impacts across the Arctic. *Nat. Ecol. Evol.* **2**, 1443–1448 (2018).
167. Schimel, D. et al. Observing terrestrial ecosystems and the carbon cycle from space. *Glob. Change Biol.* **21**, 1762–1776 (2015).
168. Park, D. S. et al. Herbarium specimens reveal substantial and unexpected variation in phenological sensitivity across the eastern United States. *Philos. Trans. R. Soc. Lond. B Biol. Sci.* **374**, 20170394 (2018).
169. Reichstein, M. et al. Deep learning and process understanding for data-driven Earth system science. *Nature* **566**, 195–204 (2019).
170. Allen, C. D. et al. A global overview of drought and heat-induced tree mortality reveals emerging climate change risks for forests. *For. Ecol. Manage.* **259**, 660–684 (2010).
171. Sturrock, R. N. et al. Climate change and forest diseases. *Plant. Pathol.* **60**, 133–149 (2011).

172. Raynolds, M. K. & Walker, D. A. Increased wetness confounds Landsat-derived NDVI trends in the central Alaska North Slope region, 1985–2011. *Environ. Res. Lett.* **11**, 085004 (2016).
173. Matasci, G. et al. Three decades of forest structural dynamics over Canada's forested ecosystems using Landsat time-series and lidar plots. *Remote. Sens. Environ.* **216**, 697–714 (2018).
174. Mitchard, E. T. A. The tropical forest carbon cycle and climate change. *Nature* **559**, 527–534 (2018).
175. Esau, I., Miles, V. V., Davy, R., Miles, M. W. & Kurchatova, A. Trends in normalized difference vegetation index (NDVI) associated with urban development in northern West Siberia. *Atmos. Chem. Phys.* **16**, 9563–9577 (2016).
176. Knyazikhin, Y. et al. Hyperspectral remote sensing of foliar nitrogen content. *Proc. Natl Acad. Sci. USA* **110**, E185–E192 (2013).
177. Tucker, C. J. Red and photographic infrared linear combinations for monitoring vegetation. *Remote. Sens. Environ.* **8**, 127–150 (1979).
178. Bannari, A., Morin, D., Bonn, F. & Huete, A. R. A review of vegetation indices. *Remote. Sens. Rev.* **13**, 95–120 (1995).
179. Myneni, R. B., Hall, F. G., Sellers, P. J. & Marshak, A. L. The interpretation of spectral vegetation indexes. *IEEE Trans. Geosci. Remote. Sens.* **33**, 481–486 (1995).
180. Xue, J. & Su, B. Significant remote sensing vegetation indices: A review of developments and applications. *J. Sens.* **2017**, 1353691 (2017).
181. Ganguly, S. et al. Generating vegetation leaf area index Earth system data record from multiple sensors. Part 2: Implementation, analysis and validation. *Remote. Sens. Environ.* **112**, 4318–4332 (2008).
182. Zhu, Z. et al. Global data sets of vegetation leaf area index (LAI) 3g and fraction of photosynthetically active radiation (FPAR) 3g derived from global inventory modeling and mapping studies (GIMMS) normalized difference vegetation index (NDVI3g) for the period 1981 to 2011. *Remote. Sens.* **5**, 927–948 (2013).
183. Pinzon, J. & Tucker, C. A non-stationary 1981–2012 AVHRR NDVI3g time series. *Remote. Sens.* **6**, 6929–6960 (2014).
Discusses complexities and challenges in detecting greenness change with the longest available NDVI dataset (AVHRR NDVI) since the 1980s.
184. Knyazikhin, Y., Martonchik, J. V., Myneni, R. B., Diner, D. J. & Running, S. W. Synergistic algorithm for estimating vegetation canopy leaf area index and fraction of absorbed photosynthetically active radiation from MODIS and MISR data. *J. Geophys. Res. Atmos.* **103**, 32257–32275 (1998).
185. Chen, J. M. & Black, T. A. Defining leaf area index for non-flat leaves. *Plant. Cell Environ.* **15**, 421–429 (1992).
186. Asrar, G. Q., Fuchs, M., Kanemasu, E. T. & Hatfield, J. L. Estimating absorbed photosynthetic radiation and leaf area index from spectral reflectance in wheat 1. *Agron. J.* **76**, 300–306 (1984).
187. Cohen, W. B., Maiersperger, T. K., Gower, S. T. & Turner, D. P. An improved strategy for regression of biophysical variables and Landsat ETM+ data. *Remote. Sens. Environ.* **84**, 561–571 (2003).
188. Baret, F. et al. GEOV1: LAI and FAPAR essential climate variables and FCOVER global time series capitalizing over existing products. Part1: Principles of development and production. *Remote. Sens. Environ.* **137**, 299–309 (2013).
189. Claverie, M., Matthews, J., Vermote, E. & Justice, C. A 30+ year AVHRR LAI and FAPAR climate data record: Algorithm description and validation. *Remote. Sens.* **8**, 263 (2016).
190. Ross, J. K. & Marshak, A. L. Calculation of canopy bidirectional reflectance using the Monte Carlo method. *Remote. Sens. Environ.* **24**, 213–225 (1988).
191. Yang, B. et al. Estimation of leaf area index and its sunlit portion from DSCOVR EPIC data: Theoretical basis. *Remote. Sens. Environ.* **198**, 69–84 (2017).
192. Xiao, Z. et al. Long-time-series global land surface satellite leaf area index product derived from MODIS and AVHRR surface reflectance. *IEEE Trans. Geosci. Remote. Sens.* **54**, 5301–5318 (2016).
193. Myneni, R., Knyazikhin, Y. & Park, T. MOD15A2H MODIS/terra leaf area index/FPAR 8-day L4 global 500 m SIN grid V006. *NASA EOSDIS L. Process. DAAC* (2015).
194. Tucker, C. J. et al. An extended AVHRR 8-km NDVI dataset compatible with MODIS and SPOT vegetation NDVI data. *Int. J. Remote. Sens.* **26**, 4485–4498 (2005).
195. Huete, A. et al. Overview of the radiometric and biophysical performance of the MODIS vegetation indices. *Remote. Sens. Environ.* **83**, 195–213 (2002).
196. Maisongrande, P., Duchemin, B. & Dedieu, G. VEGETATION/SPOT: an operational mission for the Earth monitoring; presentation of new standard products. *Int. J. Remote. Sens.* **25**, 9–14 (2004).
197. Badgley, G., Field, C. B. & Berry, J. A. Canopy near-infrared reflectance and terrestrial photosynthesis. *Sci. Adv.* **3**, e1602244 (2017).
198. Smith, W. K. et al. Large divergence of satellite and Earth system model estimates of global terrestrial CO_2 fertilization. *Nat. Clim. Change* **6**, 306–310 (2016).

Acknowledgements
This study was supported by the National Natural Science Foundation of China (41861134036, 41988101) and the Research Council of Norway (287402), the National Key R&D Program of China (2017YFA0604702), Second Tibetan Plateau Scientific Expedition and Research Program (2019QZKK0208) and the Thousand Youth Talents Plan project in China. The works of C.C., R.B.M. and T.P. were funded by NASA's Earth Science Division. R.B.M. also acknowledges support by the Alexander von Humboldt Foundation, Germany. P.C. acknowledges support by the European Research Council Synergy project (SyG- 2013-610028 IMBALANCE-P) and the ANR CLAND Convergence Institute. The authors thank Z. Zhu, Y. Li, K. Wang, Y. Deng, M. Gao and X. Li for their help in preparing the manuscript.

Author contributions
S.P., X.W., T.P., C.C., X.L., Y.H., J.W.B., A.C., P.C., H.T. and R.B.M. wrote the first draft of the manuscript. S.P., X.W. and R.B.M. reviewed and edited the manuscript before submission. All authors made substantial contributions to the discussion of content.

Competing interests
The authors declare no competing interests.

Publisher's note
Springer Nature remains neutral with regard to jurisdictional claims in published maps and institutional affiliations.

Supplementary information
Supplementary information is available for this paper at https://doi.org/10.1038/s43017-019-0001-x.

RELATED LINKS
EnMAP: http://www.enmap.org
FLEX: https://Earth.esa.int/web/guest/missions/esa-future-missions/flex
FLUXNET: https://fluxnet.fluxdata.org
HysplRI: https://hyspiri.jpl.nasa.gov
PEP725: http://www.pep725.eu
PhenoCam: http://www.phenocam.us